JOURNAL OF SPACECRAFT AND ROCKETS
Vol. 56, No. 1, January–February 2019

Drag Deorbit Device: A New Standard Reentry Actuator for CubeSats

David Guglielmo,* Sanny Omar,† and Riccardo Bevilacqua‡
University of Florida, Gainesville, Florida 32611
Laurence Fineberg,§ Justin Treptow,¶ and Bradley Poffenberger**
NASA Kennedy Space Center, Titusville, Florida 32899
and
Yusef Johnson††
a.i. solutions, Inc., Titusville, Florida 32899

DOI: 10.2514/1.A34218

The increasing number of CubeSats being launched has raised concerns about orbital debris because most of these satellites have no means of active orbit control. Some technologies exist to increase the surface area of a CubeSat and expedite deorbit due to aerodynamic drag in low Earth orbit, but most of these devices cannot be retracted, and hence cannot be used for orbital maneuvering or collision avoidance. This paper presents the drag deorbit device module that is capable of deorbiting a 12U, 15 kg CubeSat from a 700 km circular orbit in under 25 years and can be deployed and retracted to modulate the aerodynamic drag force experienced by the satellite. This facilitates the use of aerodynamic drag for orbital maneuvering, collision avoidance, and the active targeting of a deorbit location. In addition, the geometry of this drag device provides three-axis attitude stabilization of the host CubeSat using aerodynamic and gravity gradient torques, which is useful for many missions and provides a predictable aerodynamic profile for use in orbital maneuvering algorithms.

Nomenclature

A	=	cross-sectional area, m^2
a	=	semimajor axis, km
a_d	=	drag acceleration, km/s
B	=	magnetic flux density, T
B_{Earth}	=	Earth's magnetic field, T
B_r	=	magnetic remanence, T
B_s	=	magnetic saturation, T
$\dot{B}$	=	rate of change of Earth's measured magnetic field, T/s
C_b	=	ballistic coefficient
C_d	=	drag coefficient
e	=	eccentricity
H	=	magnetizing field, A/m
H_c	=	magnetic coercivity, A/m
I	=	current, A
I	=	area moment of inertia, m^4
i	=	orbital inclination, rad
J_2	=	second-order zonal harmonic of Earth's gravitational field
m	=	spacecraft mass, kg
n	=	number of turns
Q	=	heat transfer rate, J/s
r	=	Earth-centered inertial position, km
$\boldsymbol{r}$	=	Earth-centered inertial position vector, km
$\hat{s}$	=	coil normal vector
T	=	temperature, K
t	=	time, s
U	=	CubeSat standardized unit; $10 \times 10 \times 10$ cm
$\boldsymbol{v}_\infty$	=	velocity vector through a medium, km/s
ΔV	=	change in velocity required to perform an orbital maneuver, km/s
ϵ	=	emissivity
θ	=	true anomaly, rad
μ	=	magnetic dipole moment, N · m
μ_E	=	Earth gravitational parameter; $3.98574405096 * 10^{14}$ m^3/s^2
μ_0	=	permeability of free space; $1.25663706 * 10^{-6}$ $(m \cdot kg)/(s^2 \cdot A^2)$
ρ	=	atmospheric density, kg/m^3
$\boldsymbol{\tau}$	=	magnetic torque on spacecraft, N · m
Ω	=	right ascension of the ascending node, rad
ω	=	argument of periapsis, rad

Received 7 February 2018; revision received 17 May 2018; accepted for publication 20 May 2018; published online Open Access 7 September 2018.

*Postdoctoral Research Assistant, Mechanical and Aerospace Engineering Department, 939 Sweet Water Drive. Member AIAA.
†Graduate Research Assistant, Mechanical and Aerospace Engineering Department, 939 Sweet Water Drive. Student Member AIAA.
‡Associate Professor, Mechanical and Aerospace Engineering Department, 939 Sweet Water Drive. Senior Member AIAA.
§Systems and Integration Engineer, NASA Launch Services Program.
¶Flight Design Engineer, NASA Launch Services Program.
**Payload Mechanical Engineer, NASA Launch Services Program.
††Flight Design Engineer.

I. Introduction

AS MORE and more spacecraft are launched, collisions in low Earth orbit (LEO) become more likely. The potential for damage to manned spacecraft, such as the International Space Station (ISS) or crewed Soyuz vehicles, is of particular concern [1]. Many small spacecraft launch as secondary payloads and, if they have no propulsion systems, are constrained to operating in the orbit of the primary payload. CubeSats [2], which are small spacecraft primarily designed for university and research use, are a common example. Popular orbits, such as sun-synchronous orbits, have become particularly crowded due to the increasing number of CubeSats being deployed into these orbits as secondary payloads [3]. Although satellites in ISS orbits will decay relatively quickly due to aerodynamic drag, the increasing number of CubeSats deployed from the ISS has required a greater vigilance to ensure that these satellites do not interfere with or pose a collision risk to manned spacecraft or ISS resupply vehicles.

The crowding of popular low Earth orbits has led to stricter regulations on orbital debris mitigation and the desire for improved orbital maneuvering capabilities to avoid collisions between satellites. Although there is no official international policy on orbital

debris mitigation, different countries and agencies have implemented debris mitigation requirements that satellites must conform to before they are permitted to launch. For example, to further reduce the chances of collision, NASA requires that small spacecraft deorbit within 25 years, as per NASA STD-8719.14A [4]. The ESA has released similar guidelines and, as the debris problem worsens, it is likely that international regulations will one day mandate that satellite operators follow strict debris mitigation procedures. Spacecraft in high orbits can take hundreds of years to deorbit (depending on altitude and ballistic coefficient), but they cannot remain operational indefinitely. After the operational lifetime of a spacecraft has elapsed, if it has not deorbited, it becomes uncontrolled space debris. This can result in collisions between space objects, creating even more debris in a process known as the Kessler syndrome [5].

Spacecraft have traditionally been deorbited with thrusters or drag in LEO. Using drag to deorbit is a passive method, and it can be expedited by the deployment of a large aerodynamic device. Various hardware configurations have been developed, such as the Terminator Tape™ [6] and Terminator Tether™ [7], the deorbit and recovery system [8], the Gossamer Orbit Lowering Device [9], the aerodynamic end-of-life deorbit system [10], the Inflatable De-Orbit Device (iDOD) [11], the Deutsche Orbitale Servicing Mission [12], and drag sails [13–15]. Although prototypes of the Canadian Advanced Nanospace Experiment-7 (CanX-7) drag sail [14] and InflateSail [15] have flown and did indeed reduce orbit lifetime, these devices were not mass produced and are not yet reliable enough for large-scale operations. Many of the other drag devices have been unsuccessful or funding has been dropped, highlighting the need for a reliable device.

Increasing the drag sufficiently will decrease the orbit lifetime of a low-Earth-orbit (LEO) spacecraft, but the eventual deorbit location will be uncontrolled. NASA STD-8719.14A mandates that any spacecraft using controlled reentry techniques must land 370 km away from land and that the probability of targeting failure multiplied by the chance of human casualty due to the uncontrolled reentry be less than 1 in 10,000 [4]. Spacecraft containing thrusters can perform an impulsive deorbit burn to ensure that their debris lands away from populated areas, as was the case with the Delta IV upper stages [16] and the Mir space station [17]. However, a failure of the propulsion system can result in uncontrolled reentry and pose a significant hazard to persons or property on the ground, such as when Skylab fell over Australia in 1979 and generated a debris field in the Australian outback [18].

Satellites without thrusters are severely limited in their ability to perform orbital maneuvering or controlled reentry. However, differential drag techniques, or modifying the relative drag-induced acceleration between two spacecraft, have been proposed previously by Leonard in 1986 [19] as a means of thruster-free orbital maneuvering and then built upon by many researchers since then, including Maclay and Tuttle [20], Kumar and Ng [21], and Pérez and Bevilacqua [22]. By modulating the drag area of a spacecraft appropriately, the spacecraft could be made to deorbit away from populated areas without the use of any thrusters [23]. This technique could be used to save fuel for spacecraft containing thrusters and could be used to provide controlled reentry for spacecraft for which the thrusters failed or that do not contain thrusters. The variation of atmospheric drag could be performed in several different ways, including a rotation of the spacecraft panels [24] or the deployment of a drag device [25,26]. Guglielmo and Bevilacqua previously developed a repeatedly retractable drag sail that could be modulated to produce changes in the satellite drag area [26].

Regardless of the method used, some measure of attitude control is necessary to maintain a predictable drag area for aerodynamically based orbital maneuvering algorithms. A commercial off-the-shelf attitude determination and control system (ADACS) such as the Blue Canyon Technologies XACT [27], Maryland Aerospace, Inc.'s MAI-400 [28], and a unit by Clyde Space [29] are available for small spacecraft but can easily cost tens of thousands of dollars in addition to requiring significant mass and power on board the host satellite.

This paper discusses the development of a retractable drag device for small spacecraft capable of modulating the drag area while providing three-axis attitude stabilization using passive aerodynamic and gravity gradient torques and active damping using magnetorquers [30]. This drag deorbit device (D3) can be used for orbital maneuvering, collision avoidance, deorbit point targeting for spacecraft containing components that may survive reentry [23], and passive uncontrolled deorbit of spacecraft that will disintegrate on reentry. Note that the feedback control techniques discussed in Ref. [31] provide a method of continuously modulating boom deployment based on the *Global Positioning System* position and velocity measurements to ensure that a D3-equipped satellite deorbits in the desired location despite drag force uncertainties and a lack of communication with the ground. The system is unique, in that it can provide simultaneous attitude stabilization and modulation of the spacecraft's drag area, which is a capability not shared by any commercially available drag devices. The simplicity and the limited number of moving parts in the D3 system also make it a cheaper and more reliable alternative to conventional ADACS units for many satellite missions without strict pointing requirements. For example, a satellite needing to point an antenna and a camera within 20 deg of the nadir vector maintains a desired separation between sister satellites in the same orbital plane; and deorbit once its mission is complete could use the D3 exclusively as its attitude and orbit control system.

The D3 consists of four tape spring booms. Each is 3.7 m long when fully deployed, has a flat width of 4 cm, and is inclined at 20 deg relative to the rear face of the satellite. The dart configuration of these booms causes the satellite to naturally ram align due to aerodynamic forces. With attitude rate damping using magnetorquers, the D3 can cause a 12U, 15 kg satellite to ram align at altitudes of up to 700 km (circular orbit) under standard atmospheric conditions. Partially retracting two of the booms opposite to each other results in a clear minimum moment-of-inertia axis, which will simultaneously tend to align with the nadir vector due to gravity gradient torques, resulting in three-axis attitude stabilization. Five magnetorquers are used with the B-dot detumble law to damp oscillations about the equilibrium attitude. Deploying or retracting all booms simultaneously varies the aerodynamic drag force experienced by the satellite while maintaining the aerodynamically stable ram-aligned attitude. A six-degree-of-freedom (6-DOF) attitude and orbit propagator [32] was developed to assess the attitude stability of the D3 system and make design decisions about the system geometry.

This paper begins with a summary of the D3 system objectives. The hardware design presented in Sec. III is geared toward the fulfillment of these objectives. The remainder of the paper discusses the operation of this hardware and the analysis and simulations conducted to refine and validate the hardware design. Section IV discusses the modeling of the passive environmental forces and torques acting on the spacecraft that were taken into account in the 6-DOF orbit and attitude simulation. The proposed implementation of the popular B-dot magnetorquer detumble law for active attitude rate damping is discussed in Sec. V. Although many possible system configurations are tested using the simulation and control framework established up to this point, the simulation results corresponding to the final system design are presented in Sec. VI. These simulation results show that the system meets or exceeds the performance requirements. Section VII includes thermal simulations conducted by NASA Kennedy Space Center, verifying that the proposed hardware will assume acceptable temperature profiles and results from repeated testing of the deployer. Section VIII details thermal vacuum and fatigue testing with the goal of assessing the performance of the device under harsh conditions. Next, Sec. IX discusses how effectively the D3 performs its objective of reducing collision risk and minimizing orbital debris. Finally, Sec. X presents the conclusions reached during the simulation and hardware design process.

II. System Requirements

To be used as a reliable low-cost attitude and orbit control system on a variety of LEO CubeSats and potentially other small satellite missions, the D3 system is designed to meet the following requirements:

1) The D3 shall weight less than 1.33 kg and occupy a volume of less than 1U ($10 \times 10 \times 10$ cm).

2) The D3 shall integrate into a standard CubeSat structure, and the external dimensions of the device shall conform to the CubeSat standard [2].

3) The D3 must be able to successfully deorbit a 12U, 15 kg spacecraft from a 700 km circular orbit in under 25 years, assuming standard atmospheric conditions.

4) The D3 system must enable the spacecraft to maintain passive ram alignment within 15 deg up to an altitude of 700 km. This maximizes the drag area in order to expedite deorbit and provides a predictable drag profile for orbital maneuvering.

5) The D3 must be fully retractable such that the aerodynamic profile of a CubeSat with the D3 retracted is identical to the profile of that CubeSat without the D3.

6) Components of the D3 shall not create additional debris upon reentry.

7) All computing and control mechanisms required to operate the D3 shall be self-contained and capable of receiving commands from a CubeSat bus of compatible hardware.

8) D3 peak power must remain under 20 W so that it can be controlled by an unmodified, commercially available CubeSat power system. Note that the D3 is not expected to use 20 W, but this is a reasonable upper limit of what a commercial CubeSat power system could provide.

9) The angular momentum should not be transferred to the spacecraft from the D3 system during deployment.

10) The system must be able to handle at least 500 cycles of deploying and retracting without experiencing fatigue-induced failures.

III. D3 System Hardware

In keeping with the design requirements presented previously, the D3 system is designed with CubeSat compatibility in mind, although it is not restricted to CubeSat use. The maximum total projected crosswind area is 0.5 m^2, which is sufficient to deorbit a 12U, 15 kg spacecraft in 25 years under standard atmospheric conditions, and it is further discussed in Sec. VI.A. Such a spacecraft in the same ram-aligned orientation without the D3 would have an orbit lifetime of around 312 years. Four independent booms are used to achieve the D3's crosswind area, which also facilitate attitude control and provide redundancy.

A. Booms are Angled for Greater Stability

For aerodynamic stability, the booms are inclined at a 20 deg angle relative to the satellite face to which they are attached, as shown in Fig. 1. As determined by simulations, increasing the angle would result in marginally more stability, at the cost of sharply increasing the required cross-sectional area. Conversely, decreasing the angle results in a sharp decrease in stability with only a marginal increase in crosswind area. Because the D3 is intended to be used with a 12U CubeSat, the boom length is adjusted to achieve 0.5 m^2 past the crosswind area of the CubeSat. This results in a boom length of 3.7 m. Section VI elaborates further on the attitude stability properties.

B. Fabrication of Booms

The booms are rolled from 0.003-in.-thick (0.0762-mm-thick) Austenitic 316 stainless-steel stock. The initially flat stock is rolled into a rounded-V cross section to maintain its stiffness while in orbit. Using a two-roller one-pass process, three-point bending is used to achieve the desired geometry. The flat width of each piece is 40 mm, but the crosswind width is approximately 38 mm after the boom is rolled. The roller geometry is shown in Fig. 2.

Variation of the roller center-to-center distance is used to adjust the bend angle. Variation of the tip radius of curvature is used to adjust the radius of curvature of the rounded V. Nylon is used for the rollers because different versions can be iterated rapidly. Because the nylon rollers are much thicker than the stainless-steel booms, any roller deformation during the rolling process will not be significant enough to affect the final boom geometry.

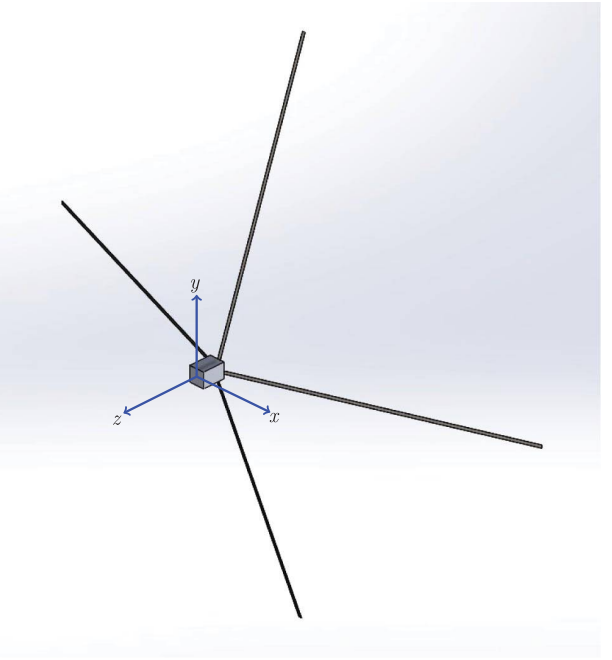

Fig. 1 D3 device attached to a CubeSat with body axes shown.

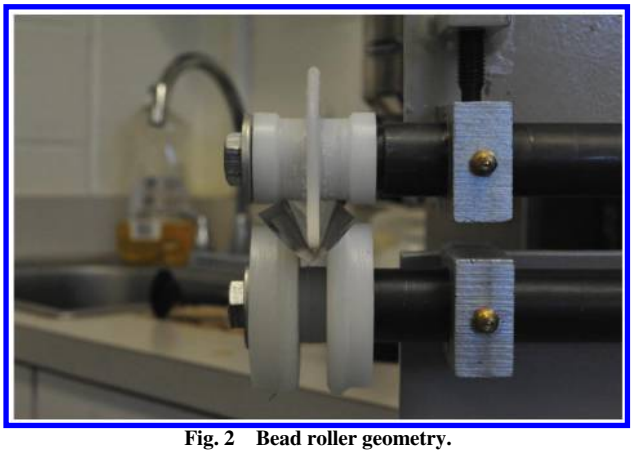

Fig. 2 Bead roller geometry.

C. Assembly and Operation of a Boom Deployer

The deployer is constructed in a manner similar to a tape measure. Each boom is first attached to a drum with four screws, as shown in Fig. 3, allowing rotation of the drum to deploy and retract the boom.

The drum is driven by a Faulhaber AM1524 stepper motor with an attached 81:1 gearbox [33]. The high reduction ratio ensures that the boom cannot backdrive the stepper, eliminating the need to power the motor when the booms are not being deployed or retracted and allowing open-loop operation.

The motor is fastened inside a sleeve, the base of which is then fastened to the outer shell as shown in Fig. 4. The drum is then fitted over the sleeve using a thrust roller bearing on each end to maintain alignment as shown in Fig. 5. Note that the drum contains a shoulder for mounting the bearing on the end closest to the gearbox output shaft.

A second shell is used to hold the deployer assembly together, with the bearing placed over the drum shoulder but inside a pocket in the shell. Four deployers are then attached to a base plate, spaced 90 deg apart as shown in Fig. 6. An expanded view of each deployer is shown in Fig. 7, where the parts indicate by each letter are listed in Table 1.

Fig. 3 Boom secured to drum.

Fig. 4 Sleeve attached to motor for later mounting.

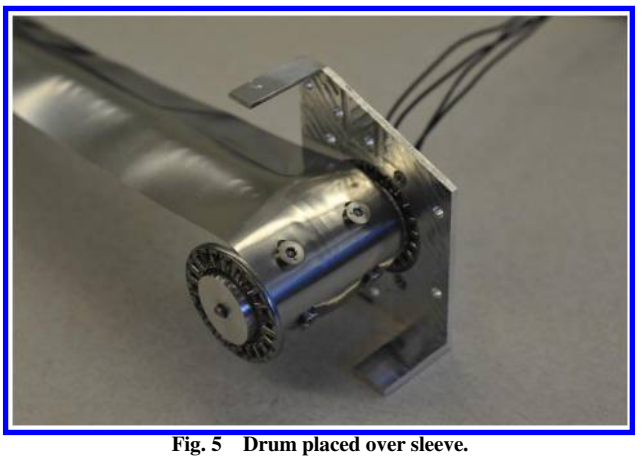

Fig. 5 Drum placed over sleeve.

D. Magnetorquer Design

For this system, the desired combined mass of all magnetorquers was approximately 100*g* and it was assumed that the magnetorquers would be supplied by a 3.3 V CubeSat power system capable of supplying up to 15 W. The magnetorquers aligned with the *x* and *y* axes (Fig. 1) would be created by wrapping coils of wire around the screw heads on the D3 deployers, whereas the *z* magnetorquer would be created by wrapping a coil of wire around the entire four-deployer assembly as shown in Fig. 6. Because there were two deployer screw assemblies facing in the *x* direction, the coils for the *x* magnetorquer would be evenly distributed among both deployers. The same applied for the *y*-magnetorquer coils. The perimeter of each loop around the deployer screw heads was 170.3 mm, and the area was 1951 mm^2.

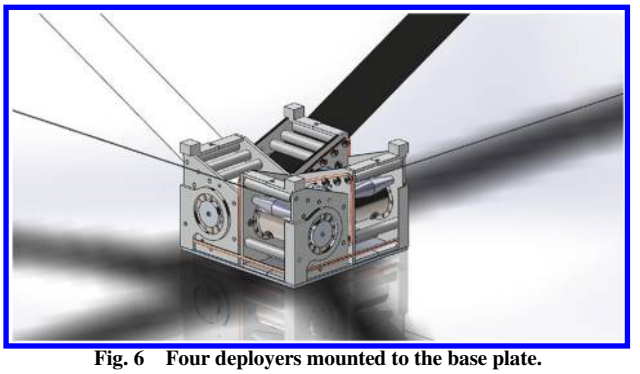

Fig. 6 Four deployers mounted to the base plate.

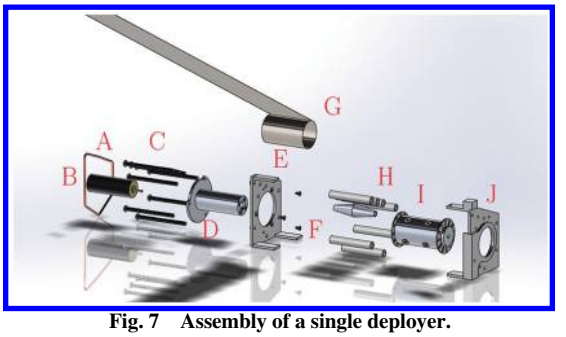

Fig. 7 Assembly of a single deployer.

The perimeter of each loop of the *z* magnetorquer was 380 mm, and the area was 9025 mm^2. By using 160 turns of 25 American wire gauge wire for the *x* and *y* magnetorquers and 40 turns for the *z* magnetorquer, the combined mass of the magnetorquers was 101 g, and the power consumption when 3.3 V was applied directly to all magnetorquers was 14.3 W. This magnetorquer design satisfied all the requirements and was capable of detumbling a 12*U*, 15 kg satellite in less than 18 h with a maximum power consumption limited to 2 W, as discussed in Sec. V.

E. D3 Hardware Control

The D3 system is controlled by a dedicated microcontroller. A BeagleBone Black controller with an AM335x 1 GHz ARM Cortex-A8 processor is used to independently control each deployer and magnetorquer. The hardware is open source and is integrated into a dedicated control board.

Four stepper controllers are used to drive the deployers, with each converting a direction and pulse input into stepper inputs. H bridges are used to control the magnetorquers.

When the spacecraft is initially deployed, the controller will first activate the B-dot magnetorquer detumble algorithm. When the spacecraft angular velocity is below a certain threshold, the controller will fully deploy the booms while running the B-dot detumble law to reduce oscillations in the attitude. Once the attitude stabilizes, the controller will stop running the B-dot law and will be ready to perform orbital maneuvering or targeted deorbit algorithms by

Table 1 Deployer components

Letter	Component
A	Magnetorquer
B	AM1524 stepper with 81:1 gearbox
C	M3-0.5 × 50 mm socket head cap screw (8x)
D	Sleeve
E	Female shell half
F	M2-0.4 × 4 mm flathead screw (3x)
G	Boom
H	Rollers (8x)
I	Drum, bearings, and M3-0.5 × 4 mm flathead screws (4x)
J	Male shell half

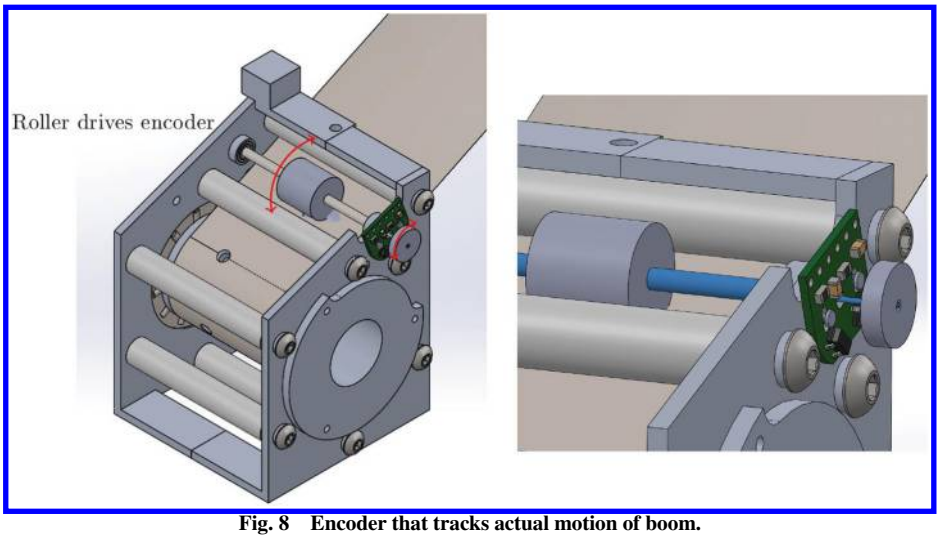

Fig. 8 Encoder that tracks actual motion of boom.

deploying and retracting the booms. The team is also considering using the space-qualified Xiphos Q7 microcontroller for satellite missions in which a higher degree of reliability is required. The Q7 has multiple copies of the operating system in different storage locations and implements active memory correction algorithms. It has been radiation tested and has significant space legacy [34].

F. Future Improvements

The control of a boom using the internal stepper motor causes the boom to intermittently wind up during the deploying and retracting processes and move in spurts instead of extending/retracting continuously. This discontinuous motion results in uncertainty on the deployed length of the boom, even if the number of motor rotations is precisely controlled. A rotary encoder is currently being considered to measure the actual deployed length by tracking the rotation of one of the rollers. A silicon roller replaces one of the polytetrafluoroethylene rollers and is used to turn the encoder wheel, as shown in Fig. 8. This roller is driven directly by the motion of the boom, and thus each rotation of the encoder corresponds precisely to a certain amount of boom deployment. Use of the encoder also allows a simple brushed motor to be used in place of the stepper motor, saving power and increasing reliability. The encoder will be used with an algorithm to control the motor and stop deployment or retraction at the appropriate point. The shaft driven by the silicon roller is shown in the rightmost drawing of Fig. 8 as the most narrow cylinder and drives the encoder wheel.

IV. Environmental Forces and Torques

Gravitational, aerodynamic, and magnetic effects impart external forces and torques on the spacecraft. The modeling of these effects is discussed in this section.

A. Aerodynamic Drag

Aerodynamic drag force is given by the equation [35]

$$\boldsymbol{F}_d = -\frac{1}{2} C_d \rho A |\boldsymbol{v}_\infty| \boldsymbol{v}_\infty \tag{1}$$

where C_d is the drag coefficient, ρ is the density, A is a reference surface area, and $\boldsymbol{v}_\infty$ is the velocity vector of the spacecraft relative to the atmosphere. Because the atmosphere rotates at approximately the same rate of the Earth, $\boldsymbol{v}_\infty$ can be calculated by [35]

$$\boldsymbol{v}_\infty = \boldsymbol{v} - \boldsymbol{\omega}_e \times \boldsymbol{r} \tag{2}$$

where $\boldsymbol{v}$ is the orbital velocity, $\boldsymbol{r}$ is the position of the spacecraft, and ω_e is the rotation rate of the Earth. Equation (1) can be divided by the spacecraft mass and rewritten to calculate the acceleration due to drag as

$$\boldsymbol{a}_d = -C_b \rho v_\infty \boldsymbol{v}_\infty \tag{3}$$

where the ballistic coefficient C_b is given by

$$C_b = \frac{C_d A}{2\ m} \tag{4}$$

The greatest uncertainty in the drag force is associated with the drag coefficient and density, although models do exist for both. For completely specular reflection in which particles do not interact with each other and they reflect off the surface at the same angle at which they impact, the theoretical drag coefficient is two for a sphere and four for a flat plate perpendicular to the velocity vector if the area used for Eq. (1) is the area of the plate or the largest cross section of the sphere [36]. The U.S. Standard Atmosphere of 1976 [37] is used to calculate the density at various altitudes to characterize the behavior of the satellite under average orbital conditions. For a specific orbit, more advanced density models such as the NRLMSISE-00 model [38] can be used for increased accuracy. Density models must take into account many factors, such as the day/night cycle, temperature, and solar and geomagnetic activities. Previous work by Guglielmo et al. showed an example of the large effect of solar and geomagnetic activities [39].

To model the total aerodynamic drag force and torque, the spacecraft can be discretized into a collection of flat plates for which the quaternion relating each plate to the spacecraft body frame is known. If specular reflection is assumed for all plates for which the angle between the surface normal vector and the velocity vector is greater than 90 deg (surface is exposed to the airstream), the component of the velocity vector perpendicular to the plate $v_\perp$ can be calculated and used with Eq. (1) to calculate the aerodynamic drag force acting at the geometric center of the plate as shown in Fig. 9. If $\boldsymbol{F}_{di}$ is the force acting on plate i and $\boldsymbol{r}_i$ is the vector from the satellite center of mass to the plate's geometric center, the total aerodynamic

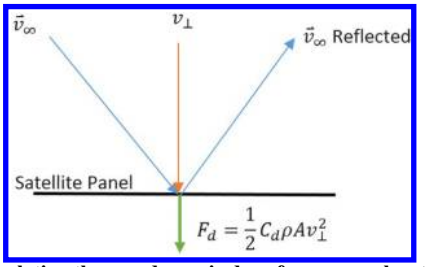

Fig. 9 Calculating the aerodynamic drag force on each satellite panel.

force $\boldsymbol{F}_{dt}$ and torque $\boldsymbol{T}_t$ acting on a satellite with n plates can be calculated by

$$\boldsymbol{F}_{dt} = \sum_{i=1}^{n} \boldsymbol{F}_{di} \tag{5}$$

$$\boldsymbol{T}_t = \sum_{i=1}^{n} \boldsymbol{r}_i \times \boldsymbol{F}_{di} \tag{6}$$

Note that this method of aerodynamic modeling does not take into account the occlusion of some panels by other panels. Techniques have been developed to account for occlusion [40], but they were not implemented in this work because the geometry of the spacecraft was such that occlusion was not a significant factor in the total aerodynamic force and torque.

B. Gravitational Effects

The Earth's gravity is by far the dominant force acting on a spacecraft in low Earth orbit. The acceleration due to Earth's gravity including J_2 was given by Bate et al. [41]. Solar and lunar gravities do have an effect, but those effects are negligible for LEO spacecraft and are not considered.

There will always be some parts of a spacecraft that are closer to the Earth than others for any given attitude. The parts closer to Earth will experience a greater gravitational attraction, resulting in a difference between the center of gravity and the center of mass. This causes a gravity gradient torque that can be written in terms of the spacecraft principal moments of inertia and the spacecraft position vector [42]. The design of the D3 ensures that, when fully deployed, the maximum moment of inertia will be about the z axis (Fig. 1) and the minimum moment of inertia will lie in the x–y plane. This means that the gravity gradient torques will help to keep the satellite ram aligned by working to ensure that the nadir vector lies in the x–y plane.

C. Magnetic Hysteresis Torques

Ferromagnetic components on board a spacecraft can easily become magnetized by the Earth's magnetic field. These components retain some of their magnetization as the spacecraft changes attitude and can interact with the Earth's magnetic field to produce a torque. This is known as magnetic hysteresis torque. Often, spacecraft with no active attitude control include hysteresis rods (long ferromagnetic rods) to reduce the spacecraft's rate of tumble. Although properly sized hysteresis rods can reduce the steady-state tumble rate, the hysteresis effect is not comparable to that of a viscous damper. Hysteresis torques sometimes add angular momentum to the spacecraft and sometimes remove it. However, the amount of angular momentum removed, on average, tends to be more than the angular momentum added when above a certain angular velocity threshold. Below this threshold, the hysteresis torques will act as a disturbance and perturb the spacecraft's attitude. For systems such as this one with long booms, making these booms out of a ferromagnetic material can cause significant hysteresis torques that may result in undesired effects. Although the fundamental physics behind magnetic hysteresis is not extremely well known, there are some mathematical techniques (based on experimental data) that can be used to characterize the hysteresis effects on a satellite and determine which materials to use. Because of the uncertainty associated with hysteresis torques and the lack of a universally accepted technique for modeling magnetic hysteresis, the methods used to simulate this phenomenon are discussed in the following. This discussion serves to highlight the assumptions made and the modeling techniques used, and it will hopefully prove useful to others who may want to simulate this effect.

The induced magnetic flux density in a metallic rod that has been exposed to some external sinusoidally varying magnetizing field is given by the hysteresis loop shown in Fig. 10, which was taken from the non-destructive testing (NDT) Resource Center [43]. When initially demagnetized and exposed to some external magnetizing field H (measured in amperes per meter), the magnetic flux density B (measured in teslas) in the rod increases until it reaches its saturation value B_s (point a on the diagram). H must then be decreased to the coercivity point H_c (point c on the diagram) for B to become zero again. If H is reduced to zero, the rod will still retain some magnetic flux density value B_r (magnetic remanence) given by point b on the diagram. Reducing H beyond H_c decreases B until saturation point $-B_c$ (point d). The cycle continues if H is increased again. The magnetic hysteresis properties of a material can be completely specified by H_c, H_r, and B_s. Note that, when the term "magnetic field" is used, the B field is what is often referred to although magnetic field has been traditionally reserved for H. As such, B will refer to the magnetic flux density and H will refer to the external magnetizing field for the purposes of hysteresis torque calculation. Magnetic field models such as the International Geomagnetic Reference Field (IGRF) [44] generally return the value of the B. B can be converted to H for use in hysteresis calculation by

$$B = \mu_0 H \tag{7}$$

where μ_0 is the permeability of free space.

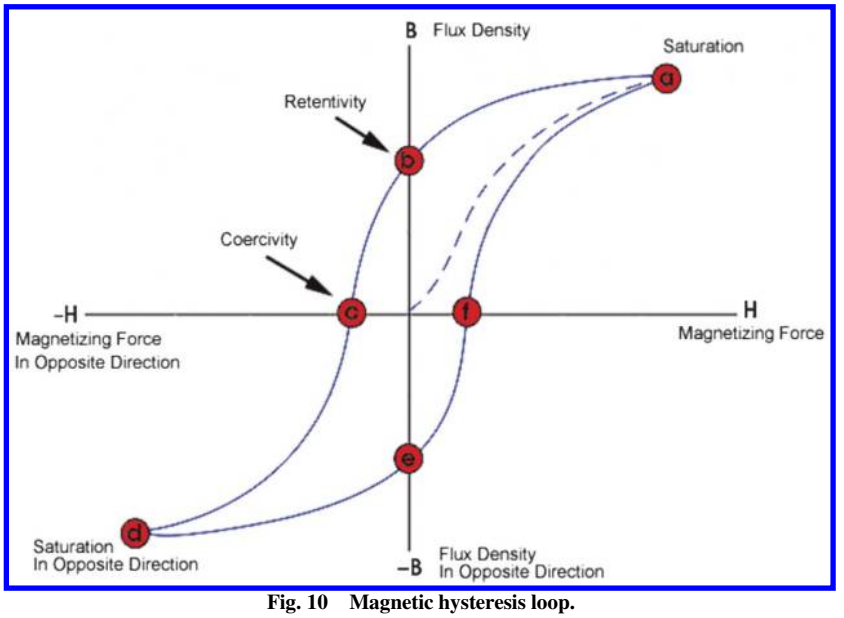

Fig. 10 Magnetic hysteresis loop.

Flatley and Henretty [45] found the arctan function to be a good fit to the hysteresis loop based on experimental data. The left boundary of the hysteresis loop can approximated by

$$B = \frac{2}{\pi} B_s \tan^{-1}[k(H + H_c)] \tag{8}$$

where B_s, B_r, and H_c are the saturation, remanence, and coercivity of the material in question; and

$$k = \frac{1}{H_c} \tan\left(\frac{\pi B_r}{2B_s}\right) \tag{9}$$

The right boundary of the hysteresis loop is similarly modeled by

$$B = \frac{2}{\pi} B_s \tan^{-1}[k(H - H_c)] \tag{10}$$

The slope of the boundary curve (either boundary) can be found by solving Eq. (8) for H, calculating the derivative with respect to H and then solving for $\mathrm{d}B/\mathrm{d}H$ [45]. This yields

$$B' = \left(\frac{\mathrm{d}B}{\mathrm{d}H}\right)_{\text{bound}} = \frac{2}{\pi} k B_s \cos^2\left(\frac{\pi B}{2B_s}\right) \tag{11}$$

Note that this value of $\mathrm{d}B/\mathrm{d}H$ is applicable only if the current value of B lies along the boundary of the hysteresis loop. There are many cases in which B may not lie along this boundary, such as when the simulation first starts with $B = 0$ and when the maximum value of H is not large enough to drive B all the way up to the saturation value of B_s. In this case, the actual value of $\mathrm{d}B/\mathrm{d}H$ can be calculated based on the boundary slope B' and the fractional distance from the corresponding boundary f:

$$\frac{\mathrm{d}B}{\mathrm{d}H} = [q_0 + (1 - q_0) f^p] B' \tag{12}$$

where q_0 and p are empirically determined constants calculated to fit the experimental data, and

$$f = \frac{|H - H_L|}{2H_c} \tag{13}$$

If $\mathrm{d}H/\mathrm{d}t$ is positive, the right boundary H_r is used in Eq. (13); whereas if $\mathrm{d}H/\mathrm{d}t$ is negative, the left boundary H_L is used in Eq. (13). With the ability to calculate $\mathrm{d}B/\mathrm{d}H$ for any values of H and B, the time rate of change of the magnetic flux density induced in the boom can be calculated as

$$\frac{\mathrm{d}B}{\mathrm{d}t} = \frac{\mathrm{d}B}{\mathrm{d}H} \frac{\mathrm{d}H}{\mathrm{d}t} \tag{14}$$

Note that $\mathrm{d}H/\mathrm{d}t$ can be calculated by first determining the rate of change of H in the satellite body frame and taking the dot product of that vector with the vector along the boom axis. In addition to the attitude quaternion and the Earth-centered inertial (ECI) position and velocity vectors, the overall state vector in the simulation can be expanded to contain the magnitude of the magnetic flux density along each boom. The aforementioned procedure can be used to calculate $\mathrm{d}B/\mathrm{d}t$ at each point in time. To simulate magnetic hysteresis, the state vector can be augmented to contain the current value of B for each boom during the numerical integration. For each boom, the magnetic moment vector can be calculated as

$$\boldsymbol{\mu} = \frac{BV\boldsymbol{l}}{\mu_0} \tag{15}$$

where V is the volume of the boom, $\boldsymbol{l}$ is the vector along the length of the boom, and μ_0 is the permeability of free space. The magnetic moments of all the booms can be summed, and the total magnetic hysteresis torque can than be calculated by

$$\boldsymbol{T}_{\text{hyst}} = \boldsymbol{\mu}_0 \times \boldsymbol{B}_{\text{Earth}} \tag{16}$$

where $\boldsymbol{B}_{\text{Earth}}$ is the magnetic field (flux density) of the Earth given directly by the IGRF model [44].

V. Active Attitude Control Using Magnetorquers

When satellites are initially deployed, they generally experience some initial angular velocity and are in a "tumbling" state. To eliminate this initial angular velocity, external torques must be applied to the satellite. This can be accomplished using the popular B-dot detumble law [30] modified to ensure that the magnetorquer power draw is within acceptable limits.

The magnetic moment vector generated by a magnetorquer is given by [46]

$$\boldsymbol{\mu} = IAn\hat{s} \tag{17}$$

where I is the current running through the magnetorquer, A is the area, n is the number of turns, and $\hat{s}$ is the unit vector normal to the coil measured in a right-handed sense such that the fingers of a right hand curl along the direction of the current if the thumb is pointing along $\hat{s}$. Assuming three orthogonal magnetorquers, a total magnetic moment vector can be created in any direction. Because magnetic torque involves a cross product of the magnetic field vector, the magnetic torque must be perpendicular to the magnetic field vector. Because magnetic torque is given by Eq. (16), the set of possible commanded magnetic moments will be restricted to values of $\boldsymbol{\mu}$ perpendicular to $\boldsymbol{B}_E$ (the magnetic field of Earth) in order to maximize the resulting torque. Selecting the direction of $\boldsymbol{\mu}$ along the ${}^E\boldsymbol{\omega}^B \times \boldsymbol{B}_E$ vector, where ${}^E\boldsymbol{\omega}^B$ is the angular velocity of the satellite body frame relative to the ECI frame, ensures that the angle between the torque vector and the projection of ${}^E\boldsymbol{\omega}^B$ onto a plane perpendicular to $\boldsymbol{B}_E$ will be 180 deg, as shown in Fig. 11 [46]. For a given magnitude of $\boldsymbol{\mu}$, this direction generates a torque vector that will serve to reduce the overall spacecraft angular momentum more than would the torque vector generated by placing $\boldsymbol{\mu}$ along any other direction. The total magnetic moment vector associated with the B-dot law can be calculated as follows:

$$\boldsymbol{\mu}_{\text{tot}} = -k\dot{\boldsymbol{B}}_E \tag{18}$$

where k is a constant gain selected based on the strength of the magnetorquers and the desired performance, and ${}^B\dot{\boldsymbol{B}}_E$ is the time rate of change of the magnetic field vector as observed in the satellite body frame given by

$${}^B\dot{\boldsymbol{B}}_E = \frac{{}^B\mathrm{d}\boldsymbol{B}_E}{\mathrm{d}t} = \boldsymbol{B}_E \times {}^E\boldsymbol{\omega}^B = \frac{\boldsymbol{B}_{E2} - \boldsymbol{B}_{E1}}{\Delta t} \tag{19}$$

In some implementations, the unit vector in the ${}^B\dot{\boldsymbol{B}}$ direction is used in Eq. (18), but the system will remain stable and effectively

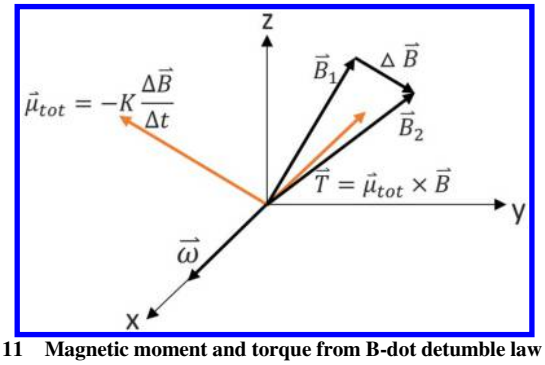

Fig. 11 Magnetic moment and torque from B-dot detumble law [46].

detumble the satellite either way. If the power P_{req} required to achieve the initially desired $\boldsymbol{\mu}_{\text{tot}_0}$ from Eq. (18) is greater than the maximum power $P_{\max}$ allocated to the B-dot law, $\boldsymbol{\mu}_{\text{tot}}$ can be reduced in magnitude to ensure that the required power is equal to $P_{\max}$ by performing the operation

$$\boldsymbol{\mu}_{\text{tot}} = \boldsymbol{\mu}_{\text{tot}_0} \sqrt{\frac{P_{\max}}{P_{\text{req}}}} \tag{20}$$

Once the current required for each magnetorquer is calculated using Eq. (17), the power required to achieve the current is given by

$$P_{\text{req}} = I^2 R \tag{21}$$

where R is the electrical resistance of the magnetorquer coil.

Unlike magnetic hysteresis torques, active magnetic control using B dot does act similarly to a velocity damper and can reduce the total spacecraft angular velocity to a very low final value (around two rotations per orbit in practice).

An aerodynamic or gravity gradient stabilized satellite with no active damping will oscillate like an undamped pendulum about the equilibrium point. In addition to detumbling the satellite, the B-dot law can also be employed as a velocity damper to reduce the amplitude of these oscillations and minimize the steady-state pointing error. The B-dot law can be deactivated once the satellite reaches its steady-state pointing behavior.

VI. Design Analysis and Simulations

Two goals of the D3 are to facilitate the deorbit of a 12U spacecraft from 700 km in 25 years and to provide a ram-aligned spacecraft attitude in order maximize the surface area perpendicular to the velocity vector, as well as to provide a predictable drag profile. The D3 also requires the ability to deploy and retract in order to perform orbital maneuvers and controlled reentry through variations in the aerodynamic drag force. Using the aforementioned modeling techniques, simulations are conducted to determine the drag device surface area required to meet the 25 year deorbit time requirement and to assess the ability of the drag device to maintain the spacecraft in a ram-aligned attitude. The theory and analysis behind these simulations are discussed here. A method of partially deploying some of the booms to achieve three-axis attitude stabilization using aerodynamic and gravity gradient forces is also investigated via simulations. In addition, this section discusses the ability of the D3 booms to maintain their rigidity and the expected accuracy with which spacecraft can be deorbited via the D3 in light of the uncertainties on the aerodynamic drag force.

A. Orbit Lifetime Analysis

The orbit lifetime of a spacecraft in LEO is directly related to the amount of aerodynamic drag the spacecraft experiences. If a spacecraft with some ballistic coefficient C_{b1} [as defined in Eq. (4)] requires some amount of time Δt_1 to deorbit from a nearly circular, the deorbit time Δt_2 for another spacecraft with the same initial conditions but a different ballistic coefficient can be estimated by

$$\Delta t_2 = \frac{C_{b1} \Delta t_1}{C_{b2}} \tag{22}$$

Equation (22) is very powerful because it allows the orbit lifetime for various satellite configurations to be estimated after conducting a single orbital simulation. Equation (22) was proven in Omar et al.'s previous work for circular orbits, in which the density was a function of the semimajor axis [23]. Although Eq. (22) is only provable for circular orbits, this is not a significant limitation because all low Earth orbits with apogees below 1000 km are approximately circular from an orbital mechanics standpoint because the apogee and perigee are defined from the center, and not the surface, of the Earth. Additionally, any low Earth orbit that is not initially circular will eventually circularize due to the increased drag at perigee.

To approximate the orbit lifetime for various initial circular orbit altitudes, a single trajectory was propagated until deorbit from an 800 km orbit with $C_{b_{\text{sim}}} = 0.1333(\text{m}^2/\text{kg})$ assuming a spherical Earth and a 1976 U.S. Standard Atmosphere for density calculations. In reality, the Earth is not a perfect sphere and the density at each altitude is not fixed, but these assumptions provide a good benchmark for a high-level analysis. Note that this large ballistic coefficient corresponding approximately to a 4 kg, 3U CubeSat equipped with a fully deployed D3 was used so that the deorbit simulation could be completed in a reasonable amount of time. After propagation was complete, Eq. (22) was used to estimate the orbit lifetimes for satellites with different ballistic coefficients (see the legend in Fig. 12). Starting the simulation from 800 km provided the orbit lifetimes for all initial circular orbit altitudes at and below 800 km.

To calculate the area of a drag device needed to deorbit a 12U (15 kg) spacecraft from 700 km in 25 years, Eq (22) was first used to

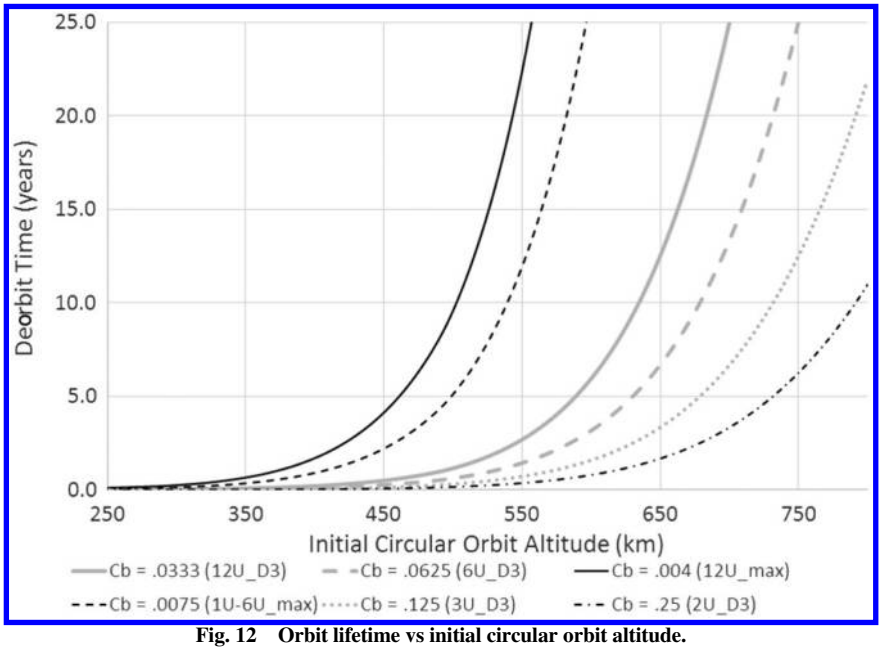

Fig. 12 Orbit lifetime vs initial circular orbit altitude.

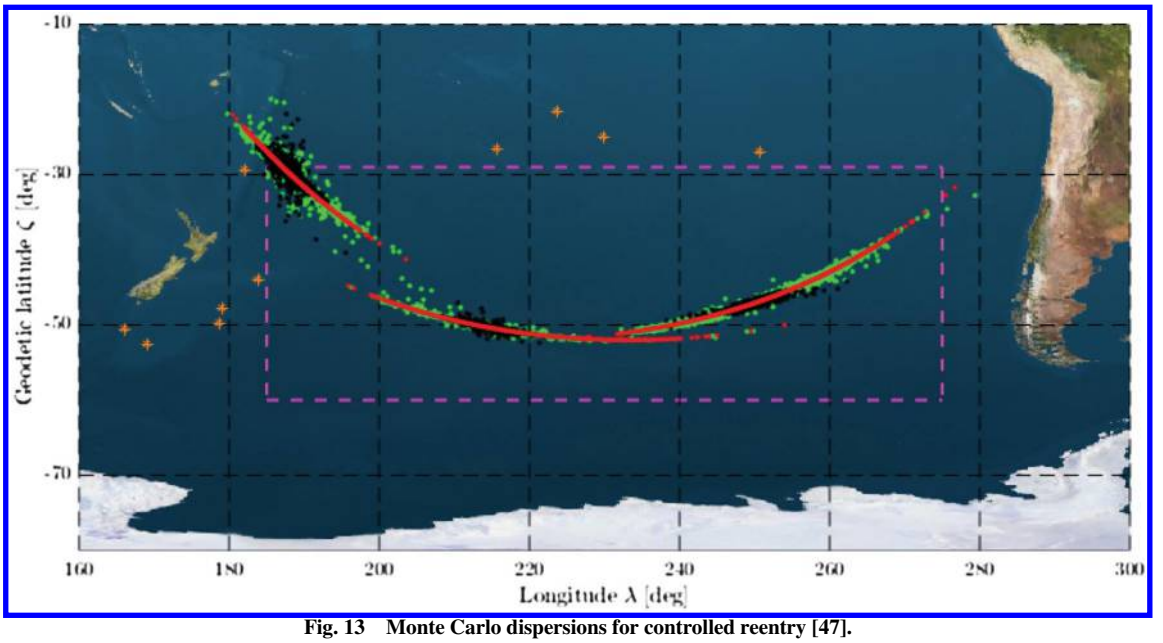

Fig. 13 Monte Carlo dispersions for controlled reentry [47].

calculate the C_b needed to deorbit from an altitude of 700 km. Given the simulated orbit lifetime of a spacecraft initially in a 700 km altitude circular orbit with $C_{b_{\text{sim}}}$, the required C_b value was

$$C_{b_{\text{req}}} = \frac{C_{b_{\text{sim}}} \Delta t_{\text{sim}}}{25\text{years}} = \frac{(0.1333)(6.25)}{25} = 0.0333 \tag{23}$$

The drag coefficient of a spacecraft in free molecular flow with completely specular reflection will range from two for a sphere to four for a flat plate [36]. Assuming a drag coefficient of two as a conservative estimate, the surface area of the drag device needed to achieve a C_b of 0.0333 for a 15 kg spacecraft can be calculated from Eq. (4) as

$$A_{\text{req}} = \frac{2C_b m}{C_d} = \frac{2(0.0333)(15)}{2} = 0.5 \text{ m}^2 \tag{24}$$

To better illustrate the expected performance of the D3 on a variety of platforms, Fig. 12 displays the orbit lifetime vs the initial altitude for spacecraft with ballistic coefficients corresponding to various geometries with and without the drag device. Included are the orbit lifetimes for 12U, 6U, 3U, and 2U satellites weighing 15, 8, 4, and 2 kg, respectively, and equipped with the drag device (area of 0.5 m^2). Also included are orbits lifetimes for 12U and 1U–6U spacecraft with no deployables oriented and with their largest faces perpendicular to velocity. Note that the drag coefficient of all spacecraft was assumed to be two as a conservative estimate. Overall, the D3 significantly reduced the orbit lifetime of nearly any legacy CubeSat configuration.

B. Boom Stiffness and Reentry Uncertainty

A key purpose of the D3 is to facilitate controlled reentry using aerodynamic drag whereby a satellite is made to deorbit in a desired location. In practice, there is significant uncertainty in the aerodynamic drag force acting on the D3 due to difficulty in modeling the drag coefficient, density, and exact boom geometry. It is shown in Ref. [31] that using Linear Quadratic Regulator (LQR)-based feedback control techniques, a D3-equipped spacecraft can track a guidance down to a geodetic altitude of 90 km with a tracking error of less than 10 km as long as it has sufficient drag controllability to do so. The guidance represents a trajectory and corresponding drag profile that, if followed, leads the satellite to a desired deorbit location. The guidance trajectory and drag profile are generated using a high-fidelity orbit propagator and the procedure used in Ref. [31]. The range of allowable guidance ballistic coefficients is set smaller than the actual range of the achievable ballistic coefficient so that the spacecraft can compensate for uncertainties in the drag force.

In practice, there will be an altitude at which the D3 booms buckle due to the aerodynamic drag force and another altitude at which reentry heating causes the onboard electronics to fail, making guidance tracking impossible. Through laboratory experimentation, it is found that 0.35 N/m of torque applied at the point where the boom exits the D3 deployer is required to make the boom buckle. To ensure that the boom does not buckle due to aerodynamic loads, the aerodynamically induced torque acting to bend the boom must not exceed 0.35 N/m by the time the boom reaches the melting altitude (approximately 92 km [47]). The guidance generation algorithm allows the user to specify the boom deployment level during the last portion of the orbit (below about 150 km). As long as the boom deployment remains below 0.35 m, the boom will not aerodynamically buckle by the altitude of 92 km. When fully deployed, the boom will buckle at about 120 km.

In Ref. [47], the reentry profile of a D3-equipped satellite was analyzed in detail. It was determined that the satellite electronics should survive to an altitude of 120 km; but, below this, the reentry temperatures became high enough to melt the electronics or at least cause them to exceed their maximum operating temperatures. To minimize the uncertainty on the boom deployment level, we found it best to set a desired boom deployment level of less than 0.3 m at a 120 km altitude and to allow the satellite to follow an uncontrolled ballistic profile for the last approximately 40 min of the orbit before ground impact. The debris footprint for the case in which the booms do not bend and the satellite performs guidance tracking down to 120 km geodetic altitude was analyzed in Ref. [47]. Figure 13 (taken from Ref. [47]) illustrates the Monte Carlo dispersions from various runs with different effects considered and guidance tracking down to an altitude of 120 km. Although spanning several thousand kilometers, the debris footprint was small enough to fit within the

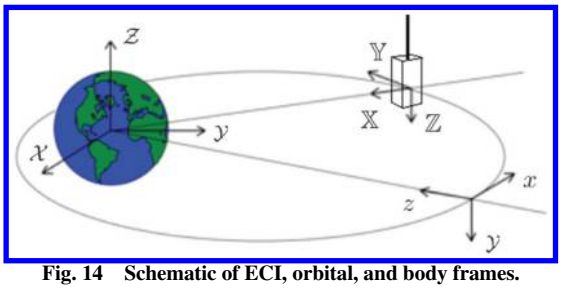

Fig. 14 Schematic of ECI, orbital, and body frames.

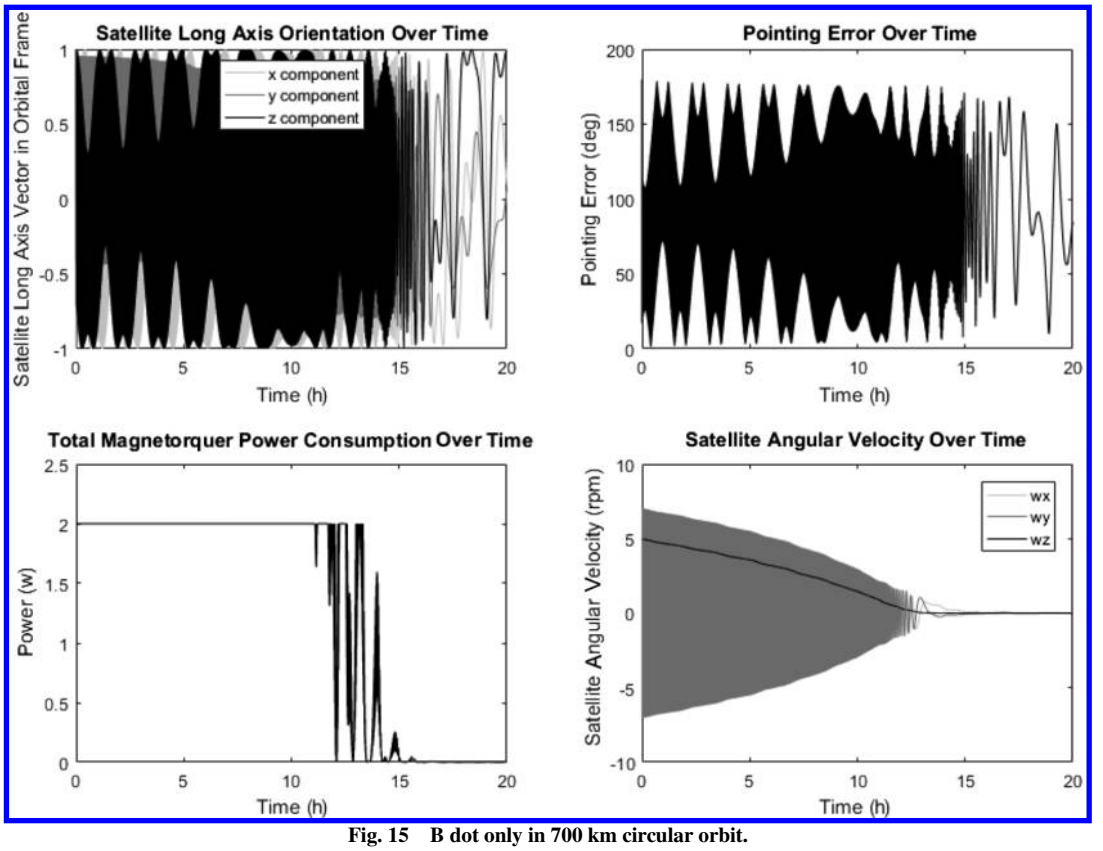

Fig. 15 B dot only in 700 km circular orbit.

south Pacific Ocean uninhabited area, which is where a satellite would likely be sent for disposal.

C. Attitude Dynamics Simulations and Results

Simulation results demonstrated that the D3 design detailed in Sec. III provided aerodynamic stability up to an altitude of 700 km. These results also showed that making the boom angle less than 20 deg significantly reduced attitude stability without appreciably increasing the surface area; whereas for angles greater than 20 deg, the decrease in surface area was not justified by the slight increase in stability. Additionally, some of the booms could be partially deployed or retracted to create a clear spacecraft minimum moment-of-inertia axis that would align with the nadir vector due to gravity gradient torques. The nonmagnetic Austenitic 316 stainless steel was selected as the material for the booms because hysteresis effects were deemed to be excessively large with ferromagnetic booms. The drag device would also contain a magnetometer and five magnetorquers in order to detumble the spacecraft and damp attitude oscillations using the B-dot detumble controller. Discussed in the following are the results of the various simulations that substantiated these decisions.

Note that, in all simulations, the attitude of the spacecraft body frame (Fig. 1) is specified with respect to the orbital frame. The orbital frame is defined as shown in Fig. 14, with its origin on the satellite center of mass such that the z points toward the Earth, the y axis is opposite the orbit angular momentum vector, and the x axis completes the right-handed coordinate system, where $x = y \times z$. In a circular orbit, the x axis is aligned with the orbit velocity vector.

1. *Detumble Phase*

The first simulation characterized the spacecraft's behavior immediately after deployment from the launch vehicle and included only magnetic torque due to the B-dot detumble controller. The satellite was assumed to have an initial tumble rate of five rotations per minute with the booms retracted. The IGRF magnetic field model of the Earth [44] was used and provided the value of the magnetic field at each time step based on the spacecraft position. Using B-dot alone, it was possible to get an angular velocity under 0.02 rpm within 12 h. In practice, B dot would remain active until the spacecraft was below a certain angular velocity threshold before deploying the booms. Figures 15 and 16 illustrate the satellite angular velocity over time when running B dot and the magnetorquer power consumption. The pointing error is defined as the angle between the satellite z axis (see Fig. 1) and the velocity vector. This error oscillates without stabilizing because there are no aerodynamic torques to align the satellite with the velocity vector. Note that the magnetorquer power consumption after the initial detumble is almost zero.

2. *Simulating Aerodynamic Stabilization*

The next simulation included magnetic torque from the B-dot algorithm, aerodynamic torques corresponding to all booms fully deployed, and gravity gradient torques corresponding to all booms fully deployed. The simulation shown in Fig. 17 illustrates the expected system performance and stability with non-ferromagnetic booms. With the booms fully deployed, the z axis of the satellite was

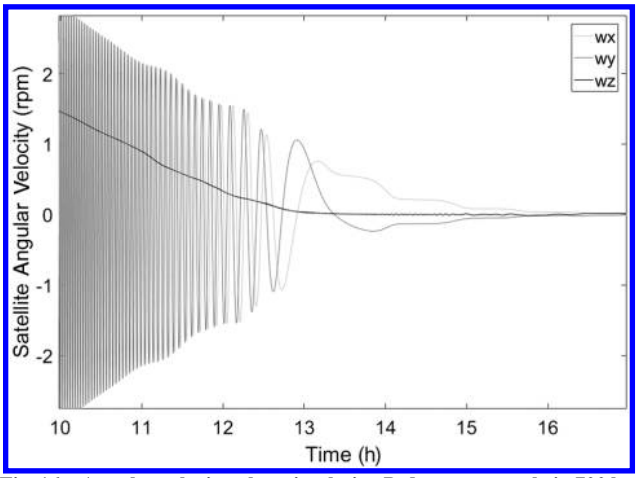

Fig. 16 Angular velocity when simulating B-dot torques only in 700 km circular orbit.

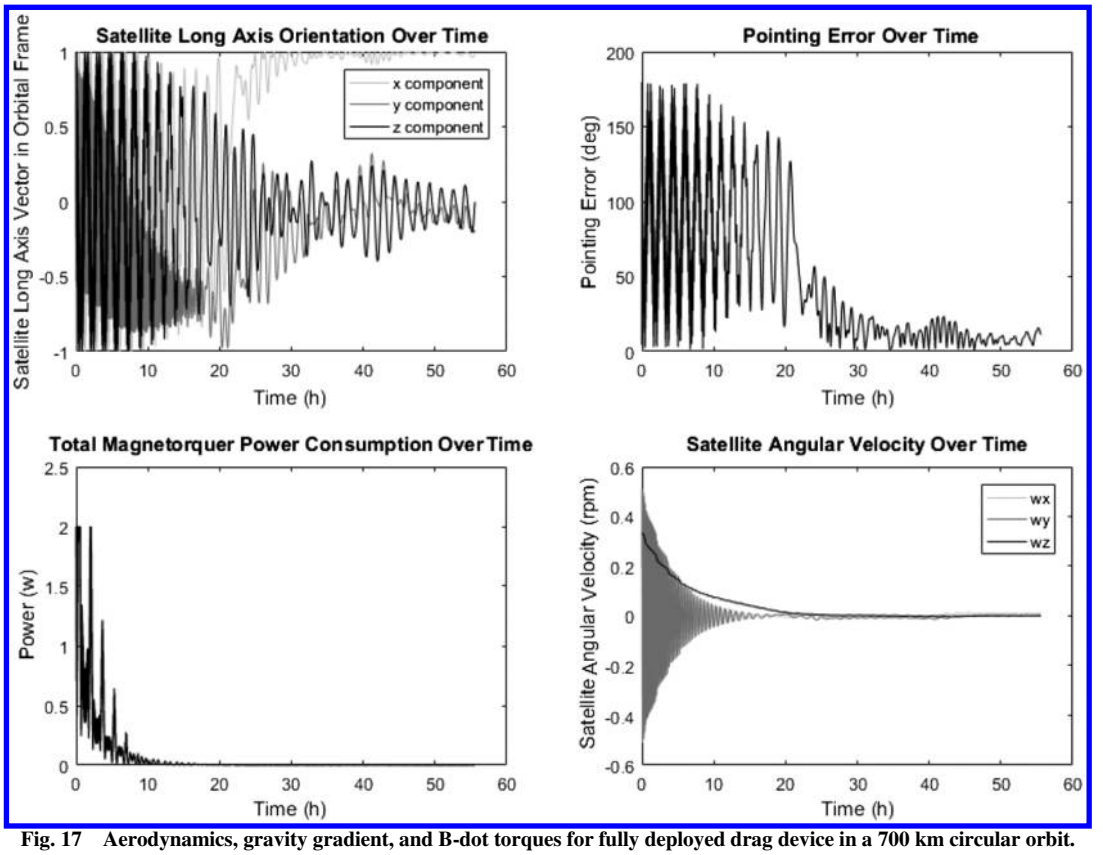

Fig. 17 Aerodynamics, gravity gradient, and B-dot torques for fully deployed drag device in a 700 km circular orbit.

the maximum moment-of-inertia axis. Because gravity gradient torques works to align the minimum moment-of-inertia axis with the nadir vector, the maximum moment-of-inertia axis must be perpendicular to the nadir vector: a constraint that helps maintain ram alignment.

3. Simulating Magnetic Hysteresis

The system from Sec. VI.C.2 was simulated with the inclusion of hysteresis torques due to the potential magnetization of the booms. Figure 18 demonstrates the hysteresis effects on booms made of wrought iron (one of the most ferromagnetic materials). As shown,

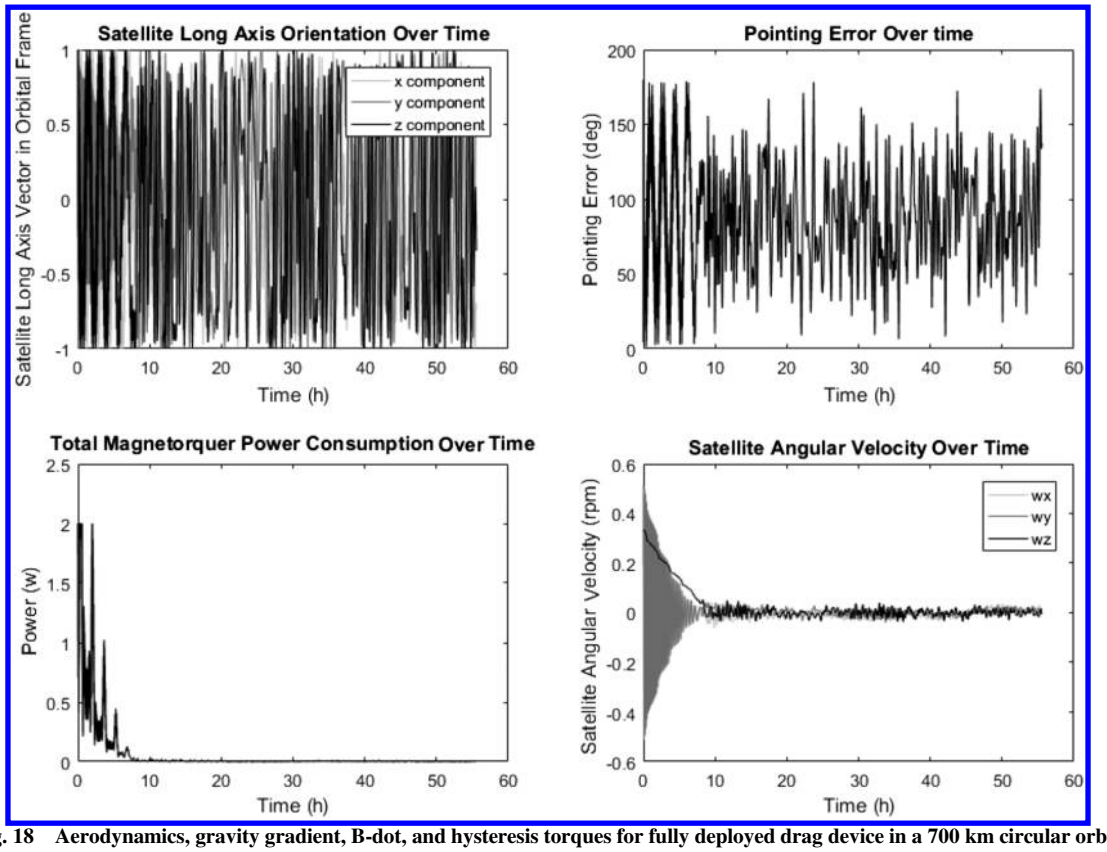

Fig. 18 Aerodynamics, gravity gradient, B-dot, and hysteresis torques for fully deployed drag device in a 700 km circular orbit.

Table 2 Average magnitudes of torques acting on satellite with fully deployed ferromagnetic booms in 400 km circular orbit

Effect	Average torque magnitude, N/m
Magnetorquer B-dot torque	1.07E-6
Gravity gradient torque	5.68E-7
Aerodynamic torque	4.34E-5
Magnetic hysteresis torque	8.52E-5

the hysteresis torques dominate the aerodynamic and gravity gradient torques and result in system instability. To characterize the magnitude of the hysteresis torques in comparison with the other torques acting on the spacecraft, a simulation is conducted of a spacecraft in a 400 km circular orbit with D3 booms, with the magnetic properties of iron fully deployed. Without hysteresis torques included in the simulation, the pointing error is less than 4 deg, but hysteresis torques cause the satellite attitude to become unstable. Table 2 shows the simulation-averaged magnitude of all torques acting on the spacecraft and illustrates the significance of hysteresis torques on long ferromagnetic booms.

This behavior is consistent with conclusions reached by other researchers through analyses and flight demonstrations that, although hysteresis torques can help reduce the initial rate of tumble, they act as disturbances in the steady state [48,49]. For this reason, the idea of using ferromagnetic booms such as premanufactured steel measuring tapes is abandoned and Austenitic 316 stainless steel is decided upon due to its ductility, low melting point as compared to other alloys of stainless steel, and low ferromagnetism.

4. Three-Axis Stabilization Using Aerodynamic and Gravity and Gradient Torques

An added benefit of having retractable booms is the ability to align one axis of the satellite with the nadir vector using gravity gradient torques. By having two booms that are opposite each other partially deployed and having the remaining two booms fully deployed, the spacecraft minimum moment-of-inertia axis will be aligned with the two fully deployed booms and will align with the nadir vector. With aerodynamic torques constraining the z axis of the satellite to align with the velocity vector, the spacecraft will be three-axis stabilized. This ability is useful if an antenna or science instrument needs to point toward the ground (nadir), away from the ground (zenith), or toward the velocity vector. Figure 19 shows the attitude dynamics when two of the booms are deployed halfway and the other two are fully deployed. Note that the graphs provide the components of each satellite body axis expressed in the orbital frame. Despite the reduction in aerodynamic torque, the spacecraft z axis aligns with the velocity vector, and the axis along the two fully deployed booms (x axis in this case) aligns with the nadir vector.

A drawback of gravity gradient stabilization is that configurations with the minimum moment-of-inertia axis aligned with either the nadir or zenith vector will be stable. However, if the satellite stabilizes in the wrong orientation, it may be possible to roll the satellite by asymmetrically deploying the booms so that the minimum moment-of-inertia axis lies 45 deg offset from its original value. After waiting for the attitude to stabilize, another 45 deg rotation can be performed. The process can be continued until the spacecraft has been rotated 180 deg to align the minimum moment-of-inertia axis with the nadir or zenith vector as desired. Alternatively, if it is desired to align the y axis with the nadir vector, the booms along the x axis can first be fully deployed and the y axis booms partially deployed such that the x axis has a minimum moment of inertia and aligns with the nadir/zenith vector. In that case, only two 45 deg rotations will be needed to align the y axis with the nadir vector. The control logic by which the booms are deployed and retracted to properly align the satellite will be investigated in future work.

VII. Thermal Simulations

A. Thermal Simulations

After completion of the preliminary design, two Thermal Desktop® simulations were used to determine the system's thermal profile. Different outer thermal coatings for the system components were considered to ensure an acceptable temperature range. A 500-km-altitude 89 deg sun-synchronous orbit was used for the

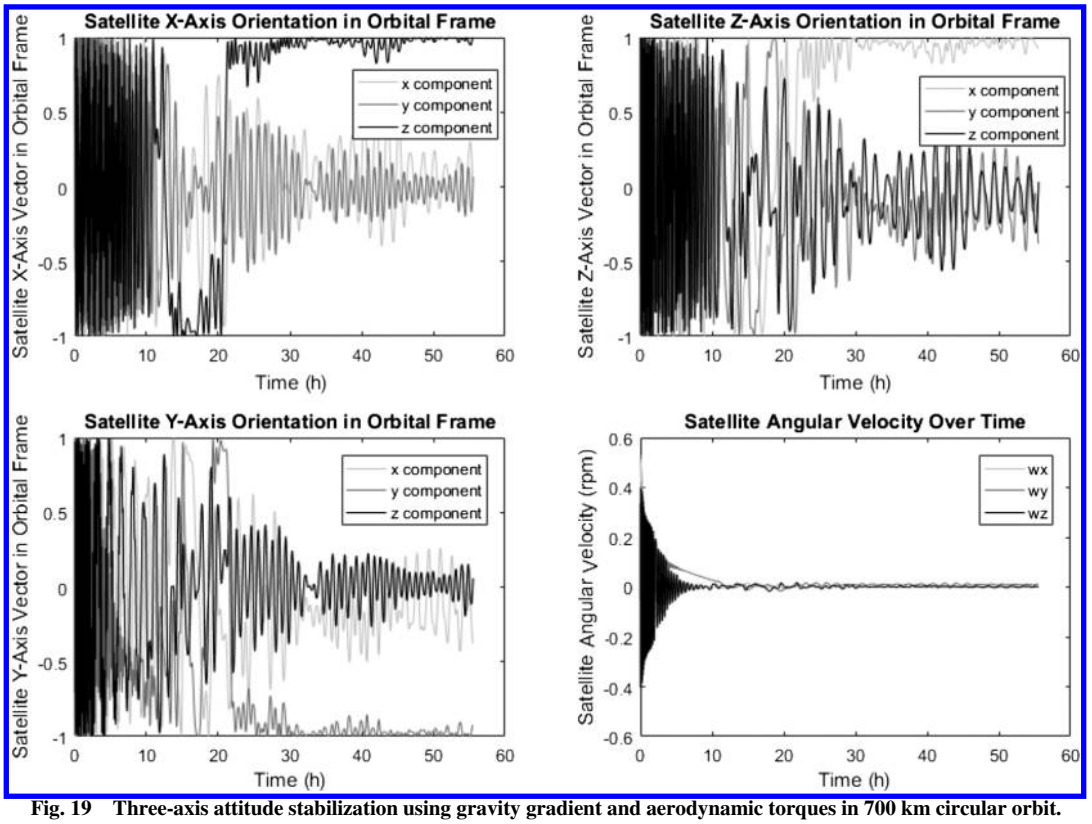

Fig. 19 Three-axis attitude stabilization using gravity gradient and aerodynamic torques in 700 km circular orbit.

Table 3 D3 materials and optical properties

Structure	Material	Surface treatment	Solar absorptivity	IR emissivity
Shell	6061 aluminum	None	0.44	0.143
Base	6061 aluminum	None	0.44	0.143
Booms	316 stainless steel	None	0.39	0.11

Table 4 D3 materials and optical properties after surface treatment

Structure	Material	Surface treatment	Solar absorptivity	IR emissivity
Shell	6061 aluminum	Anodized	0.44	0.56
Base	6061 aluminum	Anodized	0.44	0.56
Booms	316 stainless steel	Sandblasting and passivation	0.38	0.38

maximum heating case. A 500 km equatorial orbit was used as the case with maximum thermal cycling, due to the large changes in solar heating as the satellite moved in and out of eclipse.

Some simplifications were used for the thermal model. Heat transfer between the D3 outer structures and the environment, as well as conduction through the D3 major structures, have been considered. Table 3 shows the materials and surface treatments for the major parts of the system.

The temperatures of the booms and shells for both sample orbits are shown in Fig. 20. As expected, the sun-synchronous orbit showed a nearly constant temperature for both components because the heat flux was nearly constant. In comparison, the equatorial orbit showed significant temperature fluctuations, especially for the booms, as the satellite passed into and out of eclipse.

Because the D3 system and accompanying spacecraft will have several computer boards, internal temperatures must be kept within the operating ranges of these boards. The component temperatures shown in Fig. 20 would most likely result in the computer boards exceeding their operational limits and failing.

One solution to reduce the average temperatures is to anodize the aluminum components of the system, as well as combine sandblasting and passivation for the booms. The properties of these coatings are summarized in Table 4. Anodizing is an electrochemical process that can increase the emissivity of a material, leading to increased heat loss through radiation and a lower equilibrium temperature. Sandblasting involves sending a stream of abrasive particles at the stock, making the surface rougher. This will increase emissivity, at the cost of also increasing the absorptivity. To combat this, passivation is used. Passivation uses acid to remove surface contaiminants and oxidation. A new oxidation layer is formed afterward, reducing both absorptivity and emissivity, and yielding an Absorptivity to Emissivity ratio (A/E) ratio close to one. The use of black paint or a black oxide coating is also being considered to bring the A/E ratio close to one. Figure 21 shows the resulting temperature profile after the surface treatments.

B. Thermal Conclusions and Considerations

Anodizing the aluminum shells and sandblasting and passivating the booms results in boom temperatures between about −94 and 68°C and shell temperatures between 0 and 80°C, depending on the orbit. This range is acceptable for the D3 components. The board containing the onboard computer and magnetorquer and motor driver chips will be thermally isolated from the outer structure to prevent excessive thermal cycling.

Additionally, the device is intended to burn up on reentry such that no additional debris is created. The D3 components with the highest melting points are the booms made of Austenitic 316 steel, which will melt at around 1380°C. Using a reentry thermal analysis tool developed by NASA Kennedy Space Center, it was determined that the booms and all other D3 components would disintegrate completely upon reentry, even if the booms were fully coiled.

VIII. Deployer Testing

A. Repeated Cycling of Motor

To ensure the deployer would repeatedly actuate in the course of the mission, both repetition and vacuum testing were performed. The deployer was successfully cycled through its full length for 500 repetitions. This was done by deploying the boom along the length of a table as shown in Fig. 22. Because the equivalent of only a few dozen full cycles would be required in orbit, this was deemed more than sufficient. The only issue encountered while deployment testing involved the screws loosening. In practice, this would not be an issue because the screws would be held in place with epoxy while in orbit.

The deployment cycling primarily wears down the inside of the shells as shown in Fig. 23. This is due to the hard steel boom wearing the comparatively softer aluminum inner shell away. The boom tends to touch the sides of the shell during deployment; but, as the sides wear away, this becomes less of a problem. The wear on the shell is not large enough to cause any structural issues after 500 cycles.

Other wear locations could be found by searching for aluminum particles. Particles were also found in the bearings and on the inside and outside of the drum. Some wear particles were also found embedded in the rollers, but these were likely carried by the boom because there was no sliding contact between the boom and the rollers. More detailed views can be found in Fig. 24.

B. Thermal Vacuum Testing

Because the deployers were designed to work in LEO, a deployer was operated at different temperatures in a vacuum chamber. Two thermocouples were used to track the temperature. The first was placed on the motor to keep it from overheating; and the second was on the shell by the gearbox output, opposite the motor. These represented the expected hottest and coolest components,

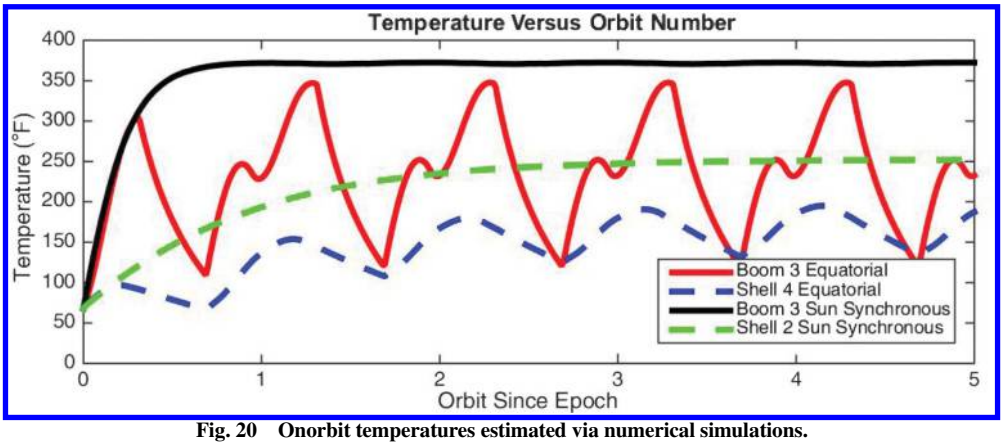

Fig. 20 Onorbit temperatures estimated via numerical simulations.

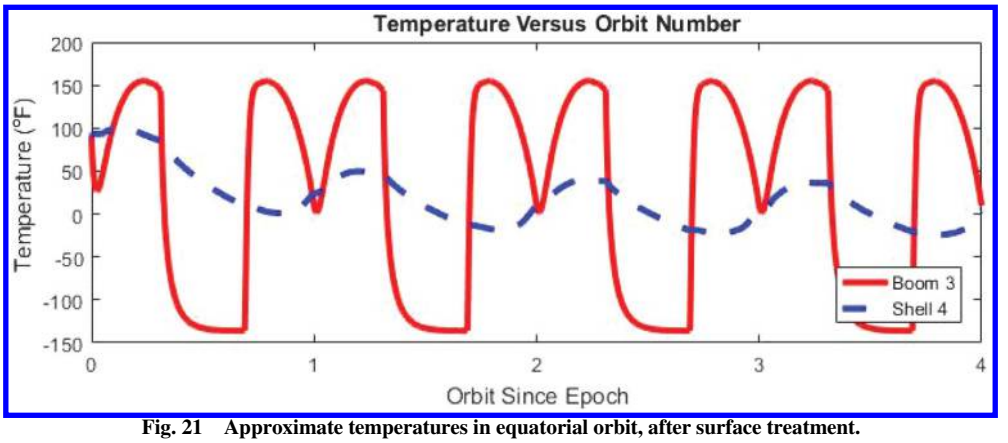

Fig. 21 Approximate temperatures in equatorial orbit, after surface treatment.

Fig. 22 Deployer extended along table.

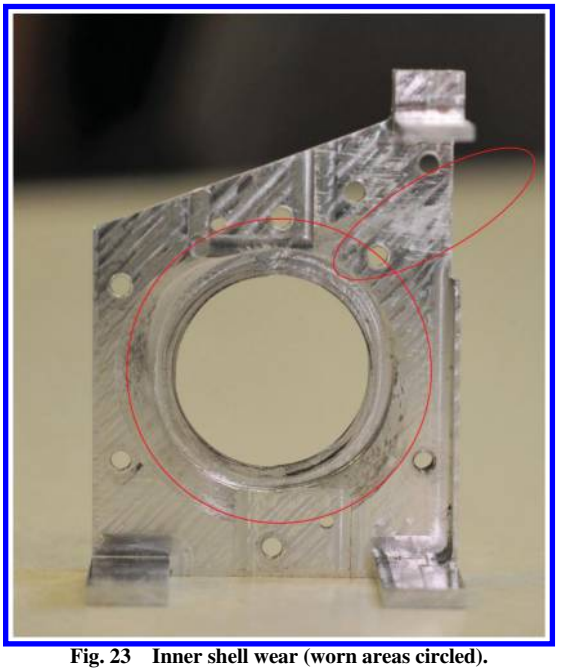

Fig. 23 Inner shell wear (worn areas circled).

respectively. The location of both thermocouples can be seen in Fig. 25.

Using the shell thermocouple as the reference point, the shell temperature was cycled to match the NASA Launch Services Program qualification test as closely as possible [50]. The shell temperature was first dropped to −5°C at a pressure of $2 * 10^{-6}$ torr, which was the lower limit of the chamber. The deployer then underwent 20 shortened deploy/retract cycles due to test chamber size limitations, or the equivalent of approximately five full cycles. Next, the temperature was raised to 55°C at a pressure of $6 * 10^{-5}$ torr, and the deployer was again taken through 20 shortened cycles.

The motor used was not vacuum rated but has been used in vacuum testing of previous iterations of the deployer. Faulhaber does, however, manufacture vacuum rated versions of this motor that will be used on the actual flight hardware. Both the high- and low-temperature cycles worked without issue. The motor experienced significant temperature rise during both cycles, rising from −1 to 70° C and from 49 to 86°C. This was within the allowable temperature range of the motor [33] and represented several continuous cycles, which would not happen in orbit. In reality, the deployer would not be actuated for more than half a cycle at a time (initial boom deployment).

The boom experienced some unexpected curvature while in the thermal vacuum chamber, curving opposite the expected direction (shown in Fig. 26). This was found to be a result of the previous testing having run along the table, putting a backward curve in the boom. Prior repeated cycling with the deployer suspended from the ceiling and the boom oriented downward to prevent backward bending did not produce any permanent deformation.

IX. Collision Risk Mitigation

The primary motivation behind the D3 and most other drag devices is to reduce orbital debris and minimize the onorbit collision risk. Equaiton (22) shows that orbit lifetime is inversely proportional to the ballistic coefficient, which increases linearly with the drag area. That is, if a drag device increases a spacecraft's cross-sectional drag area by a factor of 50, the deployment of that drag device will reduce the spacecraft's orbit lifetime by a factor of 50. If each collision object is treated as a point mass, then the collision risk per unit time is directly proportional to the spacecraft's cross-sectional area and is independent of spacecraft geometry. Thus, a factor of 50 increase in the cross-sectional area will increase the collision risk per unit time by a factor of 50, leaving the total collision risk over the life of the orbit unchanged. If the geometries of potential collision objects are considered, then the collision probability will depend on the geometry of the drag device. Long, thin deployed objects such as the D3 booms will generally increase the collision risk per unit time as compared to a square sail of identical cross-sectional area because they increase the region of space that an object with a finite volume can pass through to cause a collision.

The limited effect of classic single-deploy drag devices on collision risk raises many questions about how effective these devices are at achieving their intended goal and may be a reason why so few, if any, of these devices are commercially available. However, the D3

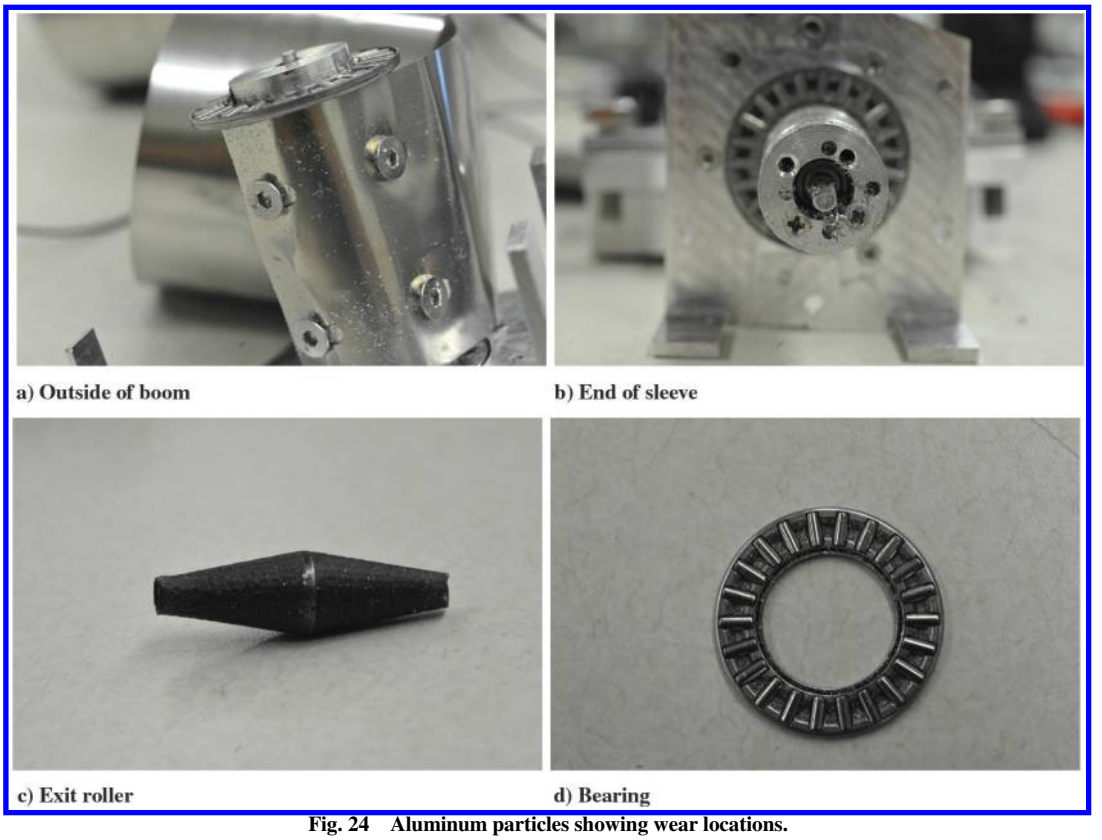

Fig. 24 Aluminum particles showing wear locations.

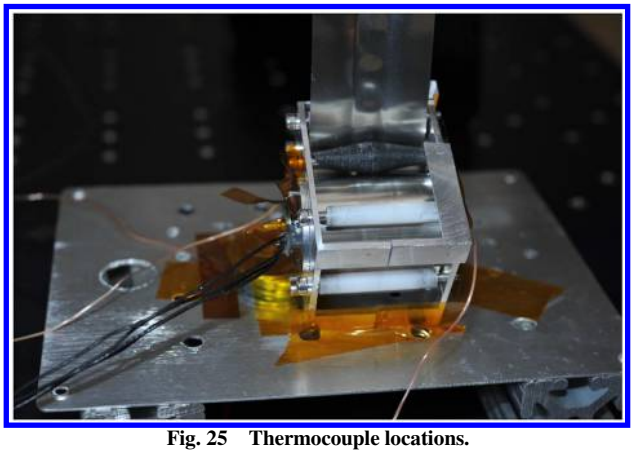

Fig. 25 Thermocouple locations.

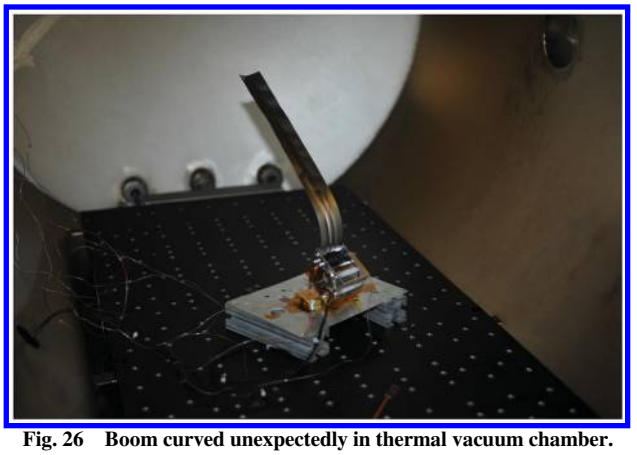

Fig. 26 Boom curved unexpectedly in thermal vacuum chamber.

device is unique in its ability to retract, and this capability makes it possible for D3-equipped satellites to substantially reduce their collision risk. If a D3-equipped satellite receives a collision warning, the satellite can, at a minimum, retract the D3 booms before the expected collision. In addition, the satellite's drag force can be modulated using the D3 to actively avoid the collision object, reducing the collision risk per unit time below that which would be expected for an identical satellite without the D3. For small, untrackable particles that can be treated as point masses, the deployment of the D3 does nothing to reduce the overall collision risk. However, it is far more likely that a collision will occur with the booms than with the main satellite body. If the D3 decreases orbit lifetime by a factor of 50, the chance of a small particle striking the main satellite is 50 times less. Although a collision with the satellite body will likely create significant shrapnel and add to the debris cloud, a collision with one of the booms will create much less debris. Small collision objects will likely punch holes in the thin booms rather than shred them.

With its ability to actively avoid large collision objects and the decreased effects of collisions with small space objects, the D3 enables small satellites to be an active part of the solution to the orbital debris problem. The onorbit collision risk can be reduced while enabling orbital maneuvering, attitude stabilization, and controlled reentry. That being said, the D3 is most effective if it is deployed and if deorbit occurs while the satellite is still operational and can actuate the D3. Deploying the D3 and abandoning the satellite for years until the deorbit time will not capitalize on the benefits of the D3 and will not appreciably reduce the collision risk.

X. Conclusions

The goal of the drag deorbit device is to reduce the collision risk and minimize the accumulation of orbital debris by enabling a 12U (15 kg) CubeSat to deorbit in 25 years from a 700 km circular orbit while providing passive attitude stability and a means of modulating the drag area for orbital maneuvering purposes. To achieve this, the

D3 is designed with four retractable tape spring booms, with each 4 cm wide (when flat), 3.7 m long, and inclined at 20 deg relative to the top face of the satellite (x–y plane), for a total drag area of 0.5 m^2. It is shown through simulations that a system in this configuration will be aerodynamically stable up to an altitude of 700 km and will align the z axis of the satellite (Fig. 1) with the velocity vector, providing a predictable attitude profile and maximizing aerodynamic drag. The booms of the drag device can also be differentially deployed such that the resulting gravity gradient torques align a satellite axis perpendicular to the z axis with the nadir vector. The ability to modulate the spacecraft's drag area by deploying and retracting the booms means that this device can be used for orbital maneuvering, collision avoidance, and the targeting of a reentry point using only aerodynamic forces. The ability to actively avoid potential collisions through drag modulation allows D3-equipped satellites to reduce their collision risk as compared to satellites with single-deploy drag sails. A thermal analysis shows that a proper surface finish applied to the booms and the boom deployer shells will ensure that all D3 components operate within their thermal limits. An additional thermal analysis also shows that the entire system will disintegrate on reentry and will not create any additional debris. Fatigue testing and thermal vacuum testing verify the ability of the D3 to function in the space environment.

The D3 is the first spacecraft subsystem capable of providing passive three-axis attitude stabilization while simultaneously modulating the drag area of the host spacecraft. On many missions, use of the D3 will eliminate the need for large, expensive, complex legacy attitude control and thruster systems. After the planned flight demonstration, the D3 has the potential to become a standard tool in orbit and attitude control, as well as debris mitigation, for small satellites.

Acknowledgments

This research was funded through the NASA Launch Services Program (subcontract 15-010) and by internal funding from the University of Florida. This work was also supported by a NASA Space Technology Research Fellowship. The authors would like to acknowledge a.i. solutions, Inc. for their help and expertise, with special mention of Scott Clark, the Program Manager of this effort. Additionally, the authors would like to thank both Glenn Lightsey of the Georgia Institute of Technology and J.-M. Wersinger of Auburn University for their help in the thermal vacuum testing.

References

[1] "IAA Situation Report on Space Debris–2016," International Academy of Astronautics TR, 2017.

[2] "CubeSat Design Specification (CDS) Rev. 13," International Astronautical Congress, Adelaide, Australia, 2017, https://static1.squarespace.com/static/5418c831e4b0fa4ecac1bacd/t/56e9b62337013b6c063a655a/1458157095454/cds_rev13_final2.pdf [retrieved 02 July 2018].

[3] Marinan, A., Nicholas, A., and Cahoy, K., "Ad-Hoc CubeSat Constellations: Secondary Launch Coverage and Distribution," *2013 IEEE Aerospace Conference*, IEEE Publ., Piscataway, NJ, March 2013. doi:10.1109/AERO.2013.6497174

[4] "Process for Limiting Orbital Debris," "NASA-STD-8719.14, Rev. A," 2011, https://standards.nasa.gov/standard/nasa/nasa-std-871914 [retrieved 2018].

[5] Kessler, D. J., and Cour-Palais, B. G., "Collision Frequency of Artificial Satellites: The Creation of a Debris Belt," *Journal of Geophysical Research*, Vol. 83, No. A6, June 1978, pp. 2637–2646. doi:10.1029/JA083iA06p02637

[6] Hoyt, R. P., Barnes, I. M., Voronka, N. R., and Slostad, J. T., "The Terminator Tape: A Cost-Effective De-Orbit Module for End-of-Life Disposal of LEO Satellites," *AIAA Space 2009 Conference*, AIAA Paper 2009-6733, 2009.

[7] Forward, R. L., Hoyt, R. P., and Uphoff, C. W., "Terminator TetherTM: A Spacecraft Deorbit Device," *Journal of Spacecraft and Rockets*, Vol. 37, No. 2, 2000, pp. 187–196. doi:10.2514/2.3565

[8] Andrews, J., Watry, K., and Brown, K., "Nanosat Deorbit and Recovery System to Enable New Missions," *Proceedings of the 2011 SmallSat Conference*, Digital Commons, Berkeley, CA, 2011.

[9] Nock, K. T., Gates, K. L., Aaron, K. M., and McRonald, A. D., "Gossamer Orbit Lowering Device (GOLD) for Safe and Efficient De-Orbit," *2010 AIAA/AAS Astrodynamic Specialist Conference*, AIAA Paper 2010-7824, 2010.

[10] Harkness, P., McRobb, M., Lützkendorf, P., Milligan, R., Feeney, A., and Clark, C., "Development Status of AEOLDOS—A Deorbit Module for Small Satellites," *Advances in Space Research*, Vol. 54, No. 1, July 2014, pp. 82–91. doi:10.1016/j.asr.2014.03.022

[11] Maessen, D. C., van Breukelen, E. D., Zandbergen, B. T. C., and Bergsma, O. K., "Development of a Generic Inflatable De-Orbit Device for CubeSats," *Proceedings of the 58th International Astronautical Congress*, ResearchGate, Berlin, 2007.

[12] Reintsema, D., Thaeter, J., Rathke, A., Naumann, W., Rank, P., and Sommer, J., "DEOS—The German Robotics Approach to Secure and De-Orbit Malfunctioned Satellites from Low Earth Orbits," *Proceedings of i-SAIRAS 2016*, ResearchGate, Berlin, 2010, pp. 244–251.

[13] E Roberts, P. C., and Harkness, P. G., "Drag Sail for End-of-Life Disposal from Low Earth Orbit," *Journal of Spacecraft and Rockets*, Vol. 44, No. 6, Nov. 2007, pp. 1195–1203. doi:10.2514/1.28626

[14] Cotton, B., Bennett, I., and Zee, R. E., "On-Orbit Results from CanX-7 Drag Sail De-Orbit Mission," SSC17-X-06, *Proceedings of the 31st Annual AIAA/USU Conference on Small Satellites*, Digital Commons, Berkeley, CA, Aug. 2017, http://digitalcommons.usu.edu/cgi/viewcontent.cgi?article=3672&context=smallsat [retrieved 2018].

[15] Viquerat, A., Schenk, M., Sanders, B., and Lappas, V. J., "Inflatable Rigidisable Mast for End-of-Life Deorbiting System," *European Conference on Spacecraft Structures, Materials and Environmental Testing (SSMET)*, Univ. of Bristol, Bristol, U.K., April 2014.

[16] Patera, R. P., Bohman, K. R., Landa, M. A., Pao, C., Urbano, R. T., Weaver, M. A., and White, D. C., "Controlled Deorbit of the Delta IV Upper Stage for the DMSP-17 Mission," *Proceedings of the 2nd IAASS Conference Space Safety in a Global World*, ResearchGate, Berlin, 2007.

[17] Luchinski, V., Murtazin, R., Sytin, O., and Ulybyshev, Y., "Mission Profile of Targeted Splashdown for Space Station Mir," *Journal of Spacecraft and Rockets*, Vol. 40, No. 5, Sept. 2003, pp. 665–671. doi:10.2514/2.6915

[18] Patera, R. P., and Ailor, W. H., "The Realities of Reentry Disposal," *Advances in Astronautical Sciences*, Vol. 99, 1998, pp. 1059–1071.

[19] Leonard, C. L., "Formationkeeping of Spacecraft via Differential Drag," M.S. Thesis, Massachusetts Inst. of Technology, Cambridge, MA, July 1986.

[20] Maclay, T. D., and Tuttle, C., "Satellite Station-Keeping of the ORBCOMM Constellation via Active Control of Atmospheric Drag: Operations, Constraints, and Performance," *Advances in the Astronautical Sciences*, Vol. 120, No. 1, 2005, pp. 763–773.

[21] Ruiter, A., Lee, J., Ng, A., Lambert, C., Hamel, J., Lafontaine, J., and Shankar, B., "Overview of Japan-Canada Joint Collaboration Satellites (JC2Sat) GNC Challenges and Design," *AIAA Guidance, Navigation, and Control Conference*, AIAA Paper 2010-7765, 2010. doi:10.2514/6.2010-7765

[22] Pérez, D., and Bevilacqua, R., "Differential Drag-Based Reference Trajectories for Spacecraft Relative Maneuvering Using Density Forecast," *Journal of Spacecraft and Rockets*, Vol. 53, No. 1, Jan. 2016, pp. 234–239. doi:10.2514/1.A33332

[23] Omar, S. R., Bevilacqua, R., Guglielmo, D., Fineberg, L., Treptow, J., Clark, S., and Johnson, Y., "Spacecraft Deorbit Point Targeting Using Aerodynamic Drag," *Journal of Guidance, Control, and Dynamics*, Vol. 40, No. 10, May 2017, pp. 2646–2652. doi:10.2514/1.G002612

[24] Bevilacqua, R., and Romano, M., "Rendezvous Maneuvers of Multiple Spacecraft Using Differential Drag Under J2 Perturbation," *Journal of Guidance, Control, and Dynamics*, Vol. 31, No. 6, Nov. 2008, pp. 1595–1607. doi:10.2514/1.36362

[25] Bevilacqua, R., "Analytical Guidance Solutions for Spacecraft Planar Rephasing via Input Shaping," *Journal of Guidance, Control, and Dynamics*, Vol. 37, No. 3, 2014, pp. 1042–1047. doi:10.2514/1.G000008

[26] Guglielmo, D., and Bevilacqua, R., "Propellant-Less Atmospheric Differential Drag LEo Spacecraft (PADDLES) Mission," *Proceedings of the 2014 SmallSat Conference*, Digital Commons, Berkeley, CA,

2014, http://riccardobevilacqua.com/Guglielmo_Student_Paper.pdf [retrieved 2018].

[27] Mason, J. P., Baumgart, M., Rogler, B., Downs, C., Williams, M., Woods, T. N., Palo, S., Chamberlin, P. C., Solomon, S., and Jones, A., et al., "MinXSS-1 CubeSat On-Orbit Pointing and Power Performance: The First Flight of the Blue Canyon Technologies XACT 3-Axis Attitude Determination and Control System," *Journal of Small Satellites*, Vol. 6, No. 3, Dec. 2017, pp. 651–662.

[28] Blackwell, W. J., Allen, G., Galbraith, C., Leslie, R., Osaretin, I., Scarito, M., Shields, M., Thompson, E., Toher, D., and Townzen, D., et al., "MicroMAS: A First Step Towards a Nanosatellite Constellation for Global Storm Observation," *Proceedings of the 2013 SmallSat Conference*, Digital Commons, Berkeley, CA, 2013.

[29] Clark, C., Viergever, K., Vick, A., and Bryson, I., "Achieving Global Awareness via Advanced Remote Sensing Techniques on 3U CubeSats," *Proceedings of the 2011 SmallSat Conference*, Digital Commons, Berkeley, CA, 2012.

[30] Lovera, M., "Magnetic Satellite Detumbling: The B-Dot Algorithm Revisited," *Proceedings of the 2015 American Control Conference (ACC)*, IEEE, New York, 2015, pp. 1867–1872. doi:10.1109/ACC.2015.7171005

[31] Omar, S., and Bevilacqua, R., "A Hybrid Adaptive Control Algorithm for Spacecraft Guidance Tracking Using Aerodynamic Drag," *Proceedings of the IAA Conference on Space Situational Awareness*, IAA Paper IAA-ICSSA-17-01-02, Nov. 2017.

[32] Hughes, P. C., *Spacecraft Attitude Dynamics*, Courier Corp., Chelmsford, MA, May 2012, pp. 93–129.

[33] "Stepper Motors," Technical Spec. AM1524-ww-ee, Dr. Fritz Faulhaber GmbH and Co. KG, Schönaich, Germany, https://www.micromo.com/media/pdfs/AM1524_FPS.PDF [retrieved July 2018].

[34] "Q7 Specifications," Xiphos Systems Corp., Quebec, http://xiphos.com/wp-content/uploads/2015/06/XTI-2001-2019-b_Q7_Spec_Sheet.pdf [retrieved July 2018].

[35] Vallado, D., *Fundamentals of Astrodynamics and Applications*, 4th ed., Microcosm Press, Hawthorne, CA, 2013.

[36] Omar, S. R., and Wersinger, J. M., "Satellite Formation Control Using Differential Drag," *53rd AIAA Aerospace Sciences Meeting*, AIAA Paper 2015-0002, 2014.

[37] "U.S. Standard Atmosphere, 1976," NASA TM-X-74335, 1976.

[38] Picone, J., Hedin, A., Drob, D., and Aikin, A., "NRLMSISE-00 Empirical Model of the Atmosphere: Statistical Comparisons and Scientific Issues," *Journal of Geophysical Research: Space Physics*, Vol. 107, No. A12, 2002, pp. SIA 15-1–SIA 15-16. doi:10.1029/2002JA009430

[39] Guglielmo, D., Pérez, D., Bevilacqua, R., and Mazal, L., "Spacecraft Relative Guidance via Spatio-Temporal Resolution in Atmospheric Density Forecasting," *Acta Astronautica*, Vol. 129, Dec. 2016, pp. 32–43. doi:10.1016/j.actaastro.2016.08.016

[40] Omar, K., and Briggs, M., "Simultaneous Orbital and Attitude Propagation of CubeSats in Low Earth Orbit," *Proceedings of the 2016 SmallSat Conference*, Digital Commons, Berkeley, CA, Aug. 2016.

[41] Bate, R. R., Mueller, D. D., and White, J. E., *Fundamentals of Astrodynamics*, Dover, New York, 1971, pp. 421–422.

[42] Curtis, H., *Orbital Mechanics for Engineering Students*, 2nd ed., Elsevier, New York, 2009, pp. 631–644.

[43] "The Hysteresis Loop and Magnetic Properties," Nondestructive Testing Resource Center, https://www.nde-ed.org/EducationResources/CommunityCollege/MagParticle/Physics/HysteresisLoop.htm [retrieved 30 July 2018].

[44] Thébault, E., et al., "International Geomagnetic Reference Field: The 12th Generation," *Earth, Planets and Space*, Vol. 67, No. 1, Dec. 2015. doi:10.1186/s40623-015-0228-9

[45] Flatley, T. W., and Henretty, D. A., "A Magnetic Hysteresis Model," NASA CP 19950021380, 1995, pp. 405–415, http://ntrs.nasa.gov/search.jsp?R=19950021380 [retrieved 2018].

[46] Omar, S., "An Inverse Dynamics Satellite Attitude Determination and Control System with Autonomous Calibration," *Proceedings of the 2015 SmallSat Conference*, Digital Commons, Berkeley, CA, Aug. 2015.

[47] Rafano Carna, S., Omar, S., Guglielmo, D., and Bevilacqua, R., "Safety Analysis for Shallow Controlled Re-Entries Through Reduced Order Modeling and Inputs' Statistics Method," *1st IAA Conference on Space Situational Awareness*, Nov. 2017.

[48] Kumar, R. R., Mazanek, D. D., and Heck, M. L., "Simulation and Shuttle Hitchhiker Validation of Passive Satellite Aerostabilization," *Journal of Spacecraft and Rockets*, Vol. 32, No. 5, Sept. 1995, pp. 806–811. doi:10.2514/3.26688

[49] Springmann, J., Kempke, B., Cutler, J., and Bahcivan, H., "Initial Flight Results of the RAX-2 Satellite," *Proceedings of the 2012 SmallSat Conference*, 2012.

[50] "Launch Services Program: Program Level Dispenser and CubeSat Requirements Document," NASA Launch Services Program Rept. LSP-REQ-317.01, Rev. B, Jan. 2014, https://www.nasa.gov/pdf/627972main_LSP-REQ-317_01A.pdf [retrieved 30 July 2018].

C. Bonnal
Associate Editor